Available online at www.sciencedirect.com
ScienceDirect
Lithos 99 (2007) 45–67
LITHOS
www.elsevier.com/locate/lithos

Xenoliths from Cerro de los Chenques (Patagonia): An example of slab-related metasomatism in the backarc lithospheric mantle

Giorgio Rivalenti [a,*], Maurizio Mazzucchelli [a], Alberto Zanetti [b], Riccardo Vannucci [b,c], Claire Bollinger [d], Christophe Hémond [d], Gustavo W. Bertotto [e]

[a] *Dipartimento di Scienze della Terra, Università di Modena e Reggio Emilia, P.le s. Eufemia 18, 41100 Modena, Italy*
[b] *CNR- Istituto di Geoscienze e Georisorse, sezione di Pavia, via Ferrata 1, 27100 Pavia, Italy*
[c] *Dipartimento di Scienze della Terra, Università di Pavia, via Ferrata 1, 27100 Pavia, Italy*
[d] *UBO-CNRS UMR 6538 Domaines Océaniques IUEM, Place Nicolas Copernic, 29290 Plouzané, France*
[e] *CONICET and Facultad de Ciencias Exactas y Naturales, Universidad Nacional de La Pampa, Uruguay 1521, 6300 Santa Rosa, La Pampa, Argentina*

Received 17 May 2006; accepted 15 May 2007
Available online 15 June 2007

Abstract

The alkali basalts of the Cerro de los Chenques quaternary backarc volcano (200 km E of the volcanic arc) carry to the surface abundant spinel-facies mantle xenoliths (lherzolites, harzburgites and dunites). The clinopyroxene geochemistry indicates that the pristine mantle was a lherzolite with Depleted Mantle (DM) composition, recording either melting episodes triggered by infiltration of a metasomatic agent or only enrichment of highly incompatible elements in those sectors where percolation occurred under decreasing fluid volume. Metasomatism was operated by a fluid originated in garnet-bearing assemblages that induced olivine and clinopyroxene dissolution, variations in the Sr and Nd isotopic signatures (i.e. pre-metasomatic mantle: $^{87}Sr/^{86}Sr=0.702712$ and $^{143}Nd/^{144}Nd=0.513495$; xenoliths recording the highest metasomatism: $^{87}Sr/^{86}Sr=0.704234$ and $^{143}Nd/^{144}Nd=0.512870$), and increase in LILE and LREE, but not in Nb and Ti. The resulting geochemical characteristics are similar to those observed in arc magmas and are consistent with the signatures of sediments and basalts forming the upper part of the subducted Nazca plate. Evidence for element fractionation operated by infiltration of the host alkali basalts and related reactive porous-flow processes are lacking or weak. The granoblastic texture of the xenoliths, bearing no evidence of deformation, rules out the hypothesis that the Chenques mantle formed in the subarc and was transported 200 km to the east by reverse corner flow. Alternatively, it is suggested that the slab components were released as supercritical fluids beneath Chenques (at ~6 GPa) by phengite breakdown. Fluids flowed through, and reacted with, the hidden garnet-facies mantle and reached the observed spinel-facies level. Reactions in the hidden mantle region led the supercritical fluid to increase $(La/Sm)_N$, Th, U, Nb, Pb and Sr while decreasing its initial $(Sm/Yb)_N$ and Ti.

Keywords: Backarc mantle lithosphere; Subducted slab fluids; Nazca Plate; Patagonia

1. Introduction

The backarc mantle lithosphere in Patagonia is abundantly sampled, from 40° to 52° latitude S and from 300 to 600 km distance from the Chile trench, by xenoliths entrained by backarc alkali basalts. These xenoliths

* Corresponding author. Tel.: +39 059 2055813.
E-mail address: riva@unimore.it (G. Rivalenti).

0024-4937/$ - see front matter © 2007 Elsevier B.V. All rights reserved.
doi:10.1016/j.lithos.2007.05.012

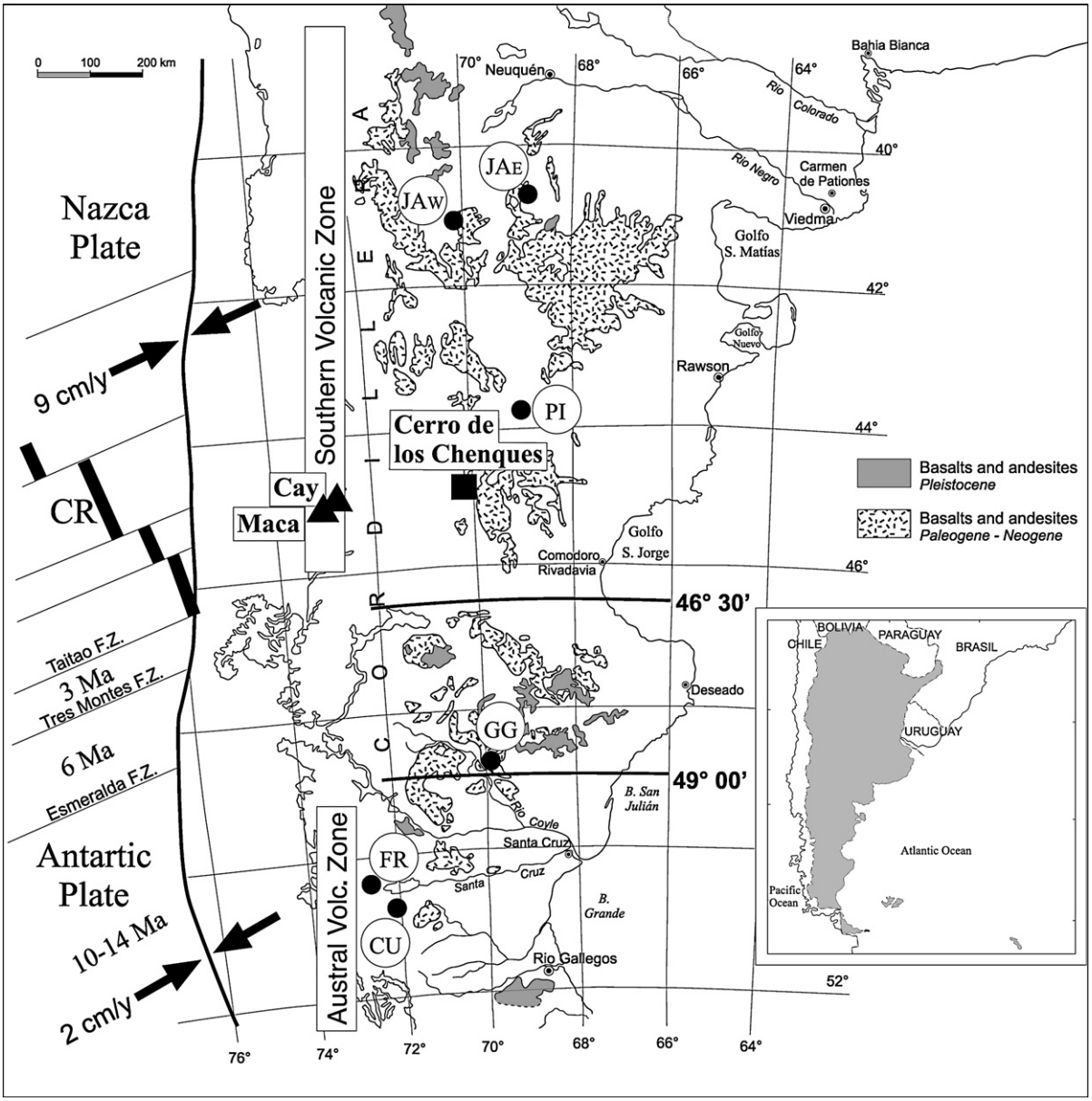

Fig. 1. Sketch map of part of Patagonia showing the Chenques locality and other xenolith occurrences mentioned in the text. The two lines at 49° and 46°30′ latitude S limit the gap in the volcanic arc. CR = Chile Ridge; JAw = Cerro del Mojon; JAe = Estancia Alvarez; PI = Paso de los Indios; GG = Gobernador Gregores; FR = El Fraile; CU = Las Cumbres.

provide an opportunity to study the regional effects of potential slab-derived components on the mantle wedge. Previous studies have shown that unequivocal evidence of slab-related metasomatism is relatively rare. This was proposed at Cerro Fraile, one of the westernmost occurrences overlaying the subduction of the Antarctic plate (Kilian et al., 1998; Kilian and Stern, 2002), possibly at Pali Aike (the southernmost occurrence, Stern et al., 1989) and at Gobernador Gregores (one of the westernmost occurrences, Laurora et al., 2001). Rivalenti et al. (2004a) also proposed that the composition of the metasomatic agents which affected the mantle wedge varied eastwards (i.e. at increasing distance from the trench) from slab-related material in the locations closer to the volcanic arc, to E-MORB like in the farthest regions, in analogy to the variations observed in the backarc plateau basalts by Stern et al. (1990), Gorring et al. (1997) and Gorring and Kay (2001). By contrast, other authors concluded that

in most cases the metasomatic agent was either a silicate melt, possibly similar to the host basalt (e.g. Pali Aike, Kempton et al., 1999; Stern et al., 1999), or a carbonatite (e.g. Gobernador Gregores, Gorring and Kay, 2000), or a plume-related component (Bjerg et al., 2005).

In this study, we revisit in detail one xenolith occurrence reported by Rivalenti et al. (2004a), namely Cerro de los Chenques (hereafter referred as Chenques). The new isotopic and geochemical data (Sr, Nd isotopic on six pyroxenes, Pb, Li and B determinations on clinopyroxenes, major and trace element composition of glass occurring in the xenoliths and the major element composition of glass-derived clinopyroxenes) provide evidence that the Chenques mantle underwent metasomatism operated by components derived from the subducted slab. This locality is important because: 1) it overlays the subducted Nazca plate and is the only one where evidence for a slab component is clear; 2) comparison with the Cerro Fraile locality may constrain differences in the metasomatic effects caused by the subduction of the Antarctic and Nazca plates; 3) it occurs immediately north of the slab window induced by the subduction of the Chile Ridge under the South America plate (Gorring et al., 1997).

2. Geological framework and information on the host basalts

The Cerro de los Chenques (latitude 44° 52′ 25″ S; longitude 70° 03′ 49″ W, Fig. 1) is an isolated, monogenetic volcano occurring about 200 km east of the Southernmost Southern Volcanic Zone (SSVZ). At this latitude, the Nazca plate is being subducted beneath South America at a rate of 8–9 cm year^{-1} (Cande and Leslie, 1986). No radiometric age determination is available, but the Chenques lavas are ascribed to the Holocene by Ploszkiewicz (1987) because they erupted over sediments of the Quaternary ice ages. Therefore, they belong to the post-plateau Quaternary volcanism (Stern et al., 1990; Gorring and Kay, 2001). In southern Patagonia, both the Neogene plateau basalts and the post-plateau lavas are inferred to derive from subslab asthenospheric sources that rose through a slab window (Gorring et al., 1997). In northern Patagonia, Kay et al. (1993a) suggested that the post-plateau lavas are related to a transient hotspot affecting a mantle previously modified by Eocenic subduction events.

The lavas hosting the xenoliths are vesicular and porphyric. The phenocrysts are olivine (Fo 78–83), clinopyroxene (Wo 38–50, Fs 9–12, En 38–42) and plagioclase (An48, Ab46, Or6). The matrix consists of olivine, plagioclase, clinopyroxene, glass, apatite and opaques (ulvospinel). The compositions of the lavas

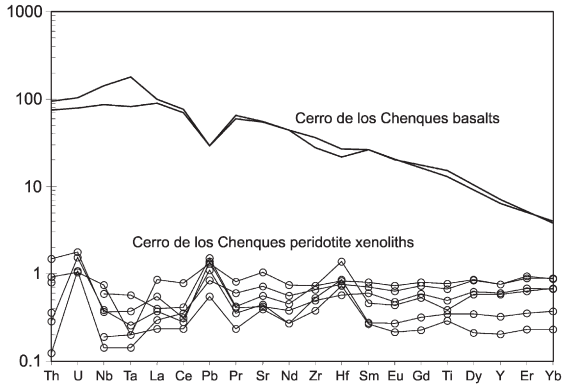

Fig. 2. Primitive mantle–normalised (Hofmann, 1988) bulk-rock trace element compositions of the Chenques basalts (sample labelled CH and PAT in Table 2 of Stern et al., 1990) and of the mantle xenoliths (Rivalenti et al., 2004a).

vary from basanite to alkali basalt. Normative nepheline ranges from 1.7–5.2%. The Mg# values [molar MgO/(MgO+FeO$_{Tot}$)] are in the range of 64–67.

Trace element concentrations, patterns and element ratios are similar to those of the cratonic basalts defined by Stern et al. (1990) (Fig. 2). Specifically, they do not display the LILE (Cs, Rb, Ba, Pb and Th) enrichment and the Nb-Ta depletion typical of lavas recording a slab imprint (Fig. 2).

3. Results from previous studies

A description of the Chenques xenoliths is provided in a regional study on the Patagonia backarc mantle lithosphere by Rivalenti et al. (2004a). The xenoliths were ejected as ellipsoidal volcanic bombs (major axis up to ~30 cm) and are coated by a lava shell. All the xenoliths are anhydrous, spinel-facies peridotites. Most are lherzolites. Harzburgites are less abundant and dunites are rare. Textures are always granoblastic and vary between the porphyroblastic and equigranular (Fig. 3). Deformation is seen only in rare kink-banded olivine and orthopyroxene crystals and evidence of sub-solidus re-equilibration is absent (exsolution lamellae in pyroxenes being very rare). Many xenoliths show host basalt infiltration as thin glass veins, which induce crystallisation of new olivine, clinopyroxene, spinel and rarely plagioclase. Although these veins are volumetrically negligible, they likely induce changes in the highly incompatible element concentrations of bulk-rock, thus not allowing their use for petrological purposes. The input from glass is, for example, likely responsible for the lack of LREE depletion in the bulk-rock trace element patterns shown in Fig. 2, although not for the positive Pb anomaly, which is absent in the basalts. In contrast, bulk-rock

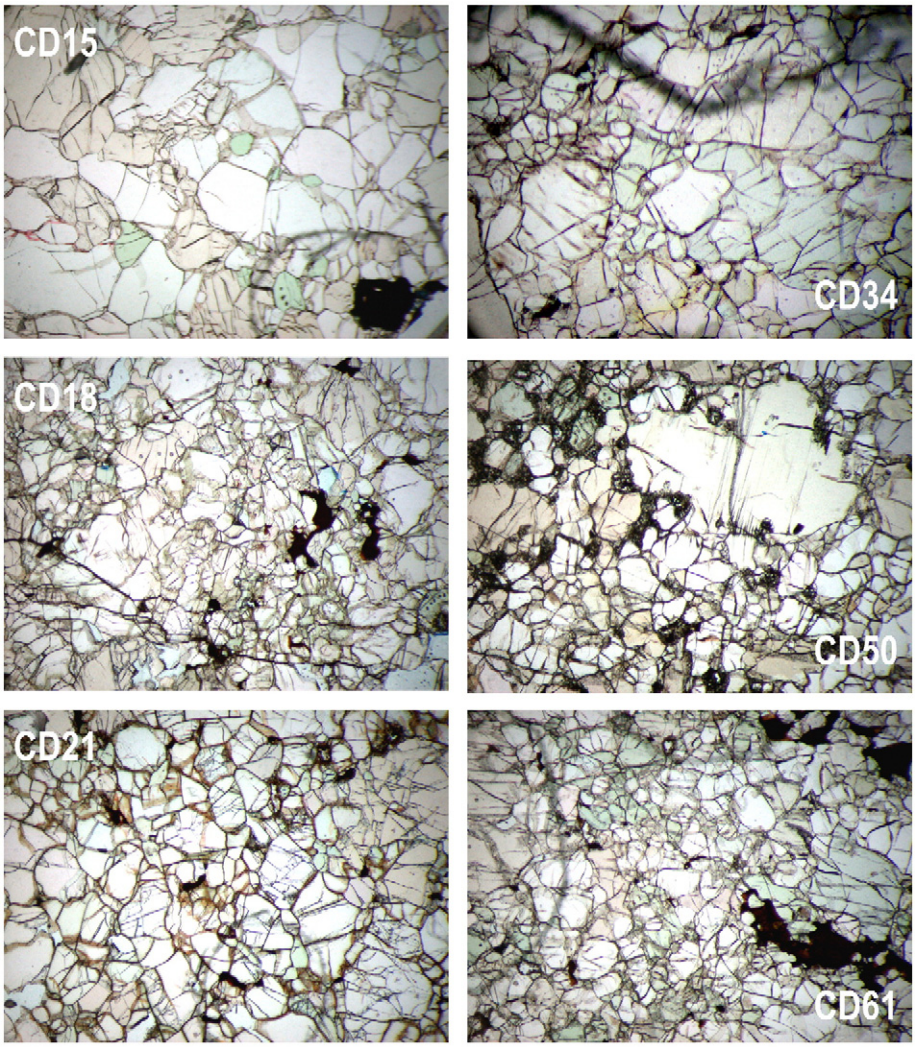

Fig. 3. Textural features of the xenoliths where isotope analysis of clinopyroxene has been made. Olivine = colourless; orthopyroxene = pale pink; clinopyroxene = green; spinel = black.

major element composition is virtually unaffected by the presence of up to 0.1% glass veins. Variations of incompatible major element contents versus MgO show negative correlations. Harzburgites are the depleted, MgO-rich, end-member of the trends.

The bulk-rock geochemical variations are accompanied by corresponding variations in the phase compositions. From lherzolites to harzburgites, the olivine composition ranges from Fo 88.2 to 91.4 and the Mg# [molar MgO/(MgO+FeO)] ranges between 89.2–92.4 in orthopyroxene, 90.5–92.9 in clinopyroxene, and 88.6–72.4 in spinel. The latter exhibits a negative correlation between Mg# and Cr# [Cr#=molar 100Cr/(Cr+Al)] within the field of the abyssal peridotite array and has very low (<0.17 wt.%) TiO_2 concentration, but harzburgites have a slightly higher TiO_2 concentration with respect to lherzolites of similar Mg# and Cr# value. In the pyroxenes, the Al_2O_3, Na_2O, TiO_2 and FeO (wt.%) concentrations decrease, and Ca increases, with increasing Mg#.

Clino- and orthopyroxenes appear to be in chemical equilibrium both for major and trace elements. The average equilibrium temperature is 1000±77 °C (Brey and Köhler. 1990, geothermometer at 1.8 GPa). The clinopyroxene geochemistry is specifically referred to in Section 5.1.

Rivalenti et al. (2004a) interpreted these xenoliths as representing a mantle section where melting-related depletion, recorded by xenoliths having LREE-depleted clinopyroxenes, was triggered by the addition of a hydrous component. The resulting melt underwent reactive porous flow into the overlaying mantle under decreasing

melt mass, as observed in the xenoliths containing variably LREE and LILE-enriched clinopyroxenes.

4. Analytical methods

Except for B and Li, and isotope determinations, the analytical methods for major and trace element determinations are reported in detail in Rivalenti et al. (2004a).

The B and Li content in clinopyroxenes, olivines, orthopyroxenes and spinels were analysed by LA–ICP–MS at the "CNR-Istituto di Geoscienze e Georisorse, Unit of Pavia". The probe is constituted by an Elan DRC-e mass spectrometer coupled with a Q-switched Nd:YAG laser source (Quantel Brilliant). The fundamental emission of the laser (1064 nm) was converted to 266 nm by two harmonic generators. Helium was used as carrier gas, mixed with Ar downstream of the ablation cell. Spot diameter was typically in the range of 40–60 μm. NIST SRM 610 glass was used as external standard. Ca content was used as an internal standard for clinopyroxene and Si for both orthopyroxene and olivine. *Routine* analyses consisted in the acquisition of background and ablated sample during one minute each. Limits of detection were at tens of ppb for Li and in the range of 100-300 ppb for B. Precision and accuracy, both better than 10% for concentrations at the ppm level, were assessed from repeated analyses of NIST SRM 612 and BCR-2g standards (Tiepolo et al., 2003, 2005).

Isotope analyses were carried out on clinopyroxene separates. The xenoliths were grinded and clinopyroxene was magnetically concentrated on the size fraction 0.1–0.2 mm and then optically handpicked. The grain size was chosen in order to exclude the clinopyroxenes related with glass, whose dimensions do not exceed 20 μm. The selected clinopyroxenes were acid-leached. Separation and analyses of Sr and Nd were performed on the same sample. Dissolution was done according to a procedure modified from White and Patchett (1984). Sr and Nd isotope ratios were measured in static mode on a Triton T1 ThermoElectron mass spectrometer at the Institut Universitaire Européen de la Mer of the Université de Bretagne Occidentale in Brest. Sr was corrected from mass fractionation to a value of 8.375209 for $^{88}Sr/^{86}Sr$ and 0.721903 for $^{146}Nd/^{144}Nd$. SRM NBS 987 and La Jolla standards during the period of the analyses had a value of 0.710253±11 (n=30) and 0.511866±9 (n=37). Nd and Sm concentrations were determined by isotope dilution using ^{148}Nd and ^{149}Sm spikes following the same separation and analytical procedure as for Nd isotopes.

Table 1
Texture, modal composition and general information on the selected samples

	CD61	CD34	CD18	CD21	CD15	CD50
Texture [a]	PF	PF	PF	GRB	GRB	PF
Mode [b]						
ol	59.6	62.7	69.2	67.0	69.8	58.8
opx	26.3	19.0	23.4	22.5	28.2	29.5
cpx	12.1	15.0	6.0	8.7	1.5	9.7
sp	1.9	3.4	1.4	1.7	0.4	1.9
glass	tr	tr	tr	tr	tr	0.20
Olivine [c]						
Fo	89.36	89.74	89.92	90.52	91.41	90.45
B ppm	0.4±0.1				0.5±0.1	1.4±0.1
Li ppm	2.0±0.5		1.7±0.2	1.6±0.1	1.4±0.1	1.8±0.2
Orthopyroxene [c]						
Mg#	90.43	90.45	90.43	91.00	92.37	91.00
Al_2O_3 wt.%	3.69	3.56	3.33	3.38	2.14	3.08
B	0.5±0.1		0.5±0.1	0.8±0.1	0.6±0.1	1.7±0.2
Li	1.2±0.1		1.2±0.2	0.4±0.2	0.7±0.1	1.0±0.2
Spinel						
Mg#	78.06	80.96	72.53	68.39	43.32	68.21
Cr#	10.91	9.49	14.80	18.16	47.14	17.76
TiO_2 wt.%	0.01	0.05	0.10	0.11	0.10	0.05
Temperature [d]	968	907	890	916	993	896

[a] PF = porphyroblastic GRB = granoblastic.
[b] In weight %; tr = trace.
[c] 1σ standard deviation in Li and B.
[d] Brey and Köhler (1990) at 1.8 GPa.

Table 2
Major, trace element, Sr and Nd isotope analyses and 1σ standard deviation (italic) for the selected clinopyroxenes

	CD61		CD34		CD18		CD21		CD15		CD50	
wt.%[a]												
SiO_2	52.65	*0.15*	52.04	*0.12*	52.90	*0.10*	52.96	*0.05*	53.88	*0.09*	53.29	*0.11*
TiO_2	0.47	*0.02*	0.35	*0.03*	0.50	*0.02*	0.31	*0.03*	0.07	*0.06*	0.16	*0.02*
Al_2O_3	6.26	*0.17*	5.30	*0.14*	5.74	*0.16*	4.75	*0.11*	3.58	*0.01*	3.90	*0.11*
Cr_2O_3	0.87	*0.06*	0.60	*0.04*	0.97	*0.08*	0.89	*0.02*	1.95	*0.09*	0.75	*0.07*
FeO	2.55	*0.05*	2.46	*0.01*	2.46	*0.09*	2.28	*0.07*	2.19	*0.09*	2.28	*0.05*
MnO	0.09	*0.03*	0.07	*0.09*	0.07	*0.03*	0.09	*0.01*	0.08	*0.07*	0.08	*0.04*
MgO	15.09	*0.23*	14.99	*0.13*	14.75	*0.11*	15.62	*0.20*	16.14	*0.02*	16.35	*0.07*
CaO	20.23	*0.22*	22.03	*0.04*	20.74	*0.24*	21.65	*0.22*	20.50	*0.22*	22.29	*0.14*
Na2O	1.76	*0.05*	1.55	*0.08*	1.84	*0.06*	1.23	*0.03*	1.59	*0.26*	0.87	*0.04*
Mg#	91.33	*2.81*	91.62	*1.54*	91.45	*1.60*	92.43	*2.44*	92.93	*0.52*	92.74	*0.92*
ppm[b]												
Li	1.0	*0.32*	1.4	*0.13*	0.7	*0.21*	1.1	*0.08*	0.9	*0.09*	0.8	*0.13*
B	0.4	*0.03*	0.5	*0.13*	0.5	*0.16*	0.4	*0.18*	0.6	*0.05*	1.5	*0.13*
Sc	62.6	*1.8*	63.2	*2.0*	72.2	*2.3*	64.6	*2.7*	79.4	*0.2*	55.3	*1.9*
Ti	2561	*127*	1941	*166*	3149	*350*	1612	*18*	326	*15*	921	*49*
V	273	*4*	253	*4*	302	*7*	240	*12*	244	*5*	186	*9*
Sr	41.0	*2.0*	83.0	*8.5*	89.5	*4.7*	44.6	*0.4*	303.1	*19.5*	155.5	*7.2*
Y	16.7	*1.3*	14.9	*0.3*	16.7	*2.0*	11.1	*0.9*	9.5	*0.8*	10.4	*0.4*
Zr	21.2	*1.6*	25.3	*0.4*	49.2	*5.1*	17.3	*1.1*	103.4	*7.8*	38.5	*7.0*

Nb	0.030	*0.002*	0.110	*0.030*	0.197	*0.047*	0.035	*0.005*	0.761	*0.029*	0.068	*0.027*
La	0.445	*0.040*	3.570	*0.340*	1.915	*0.157*	0.742	*0.012*	13.255	*1.018*	4.201	*0.117*
Ce	1.964	*0.057*	6.870	*1.270*	5.956	*0.505*	2.829	*0.125*	29.798	*2.825*	11.119	*0.493*
Pr	0.428	*0.019*	0.810	*0.150*	0.947	*0.088*	0.501	*0.026*	3.146	*0.492*	1.488	*0.090*
Nd	2.717	*0.112*	3.860	*0.490*	4.690	*0.410*	2.688	*0.157*	10.317	*0.616*	6.237	*0.494*
Sm	1.372	*0.119*	1.360	*0.160*	1.761	*0.164*	1.002	*0.049*	2.598	*0.150*	1.513	*0.115*
Eu	0.611	*0.029*	0.593	*0.060*	0.718	*0.063*	0.409	*0.007*	0.806	*0.067*	0.566	*0.053*
Gd	2.074	*0.138*	1.988	*0.230*	2.281	*0.185*	1.361	*0.017*	2.258	*0.141*	1.506	*0.051*
Dy	2.726	*0.192*	2.550	*0.220*	2.809	*0.301*	1.688	*0.054*	2.041	*0.084*	1.708	*0.083*
Er	1.728	*0.076*	1.640	*0.110*	1.704	*0.160*	1.033	*0.049*	0.879	*0.041*	1.053	*0.110*
Yb	1.675	*0.156*	1.564	*0.167*	1.694	*0.181*	1.028	*0.039*	0.535	*0.093*	1.125	*0.089*
Hf	0.658	*0.055*	0.830	*0.090*	1.460	*0.073*	0.531	*0.009*	2.272	*0.240*	0.608	*0.122*
Ta	0.012	*0.015*	0.018	*0.009*	0.130	*0.016*			0.083	*0.008*		
Pb	0.093	*0.030*	0.270	*0.030*	0.193	*0.032*	0.108	*0.023*	0.840	*0.089*	0.408	*0.088*
Th	0.021	*0.003*	0.200	*0.020*	0.430	*0.046*	0.029	*0.003*	1.201	*0.052*	1.015	*0.096*
U	0.007	*0.001*	0.093	*0.011*	0.146	*0.013*	0.010	*0.003*	0.431	*0.011*	0.247	*0.025*
147Sm/144Nd[b]	0.304	*0.039*	0.212	*0.052*	0.226	*0.041*	0.224	*0.024*	0.152	*0.018*	0.146	*0.023*
147Sm/144Nd[c]	0.2642	*0.0053*	0.2029	*0.0041*	0.2136	*0.0043*	0.2330	*0.0047*	0.1354	*0.0027*	0.1488	*0.0030*
143Nd/144Nd	0.513495	*0.000007*	0.512942	*0.000005*	0.513134	*0.000006*	0.513007	*0.000006*	0.512870	*0.000006*	0.512788	*0.000006*
87Sr/86Sr	0.702712	*0.000008*	0.703592	*0.000005*	0.702786	*0.000007*	0.703319	*0.000005*	0.704234	*0.000008*	0.704145	*0.000007*

Major and trace element data are from Rivalenti et al. (2004a). Isotopes and Pb, Li, B and CD34 trace element composition are new data.

[a] Electron microprobe analyses.

[b] LA–ICP–MS analyses.

[c] Isotopic dilution analyses.

5. Petrography and geochemistry of the selected samples

Samples were selected on the basis of their dimension (large enough to permit clinopyroxene separation for isotope analysis) and geochemical variability of clinopyroxene (that need to cover the entire variation observed at Chenques). The textural characteristics and modal composition of the selected xenoliths are summarized in Table 1, along with composition of the main phases, and illustrated in Fig. 3. All the samples have a granoblastic texture and only CD50 contains visible glass veins (0.2 wt.%). The sample compositions vary between lherzolite (CD34, CD61), variably cpx-poor lherzolites (CD50, CD21 and CD18) and harzburgite (CD15).

5.1. Clinopyroxene geochemistry

Representative analyses of clinopyroxene cores from the selected samples are reported in Table 2 and compared with the larger data set of Rivalenti et al. (2004a) in Figs. 4 and 5. The Mg# values are in the range of 91.3 (lherzolite CD61)–92.9 (harzburgite CD15). The TiO_2, Al_2O_3, FeO and Na_2O concentrations decrease, and the CaO concentration increases, when Mg# increases. The clinopyroxene of the harzburgite CD15 plots off the Na_2O and CaO variation trend for having a much higher Na_2O (Fig. 4) and lower CaO (not shown) concentrations. The composition of the matrix clinopyroxenes is compared in Fig. 4 with that of clinopyroxenes crystallized from the glass veins and pockets. Within the same Mg# range, the glass-related clinopyroxenes have higher TiO_2, Al_2O_3, FeO and lower Na_2O concentrations.

For convenience of description, we put the matrix clinopyroxenes into three groups on the basis of their trace element patterns. Fig. 5 shows that the selected samples document all the groups and their internal variations.

Group 1 is characterized by flat at ~4xPM (Primitive mantle, Hofmann, 1988) concentration from Sm to Yb and by variable LREE-depletion (e.g., CD 61, $(La/Yb)_N$= 0.2) to LREE-enrichment (e.g., CD 34, $(La/Nd)_N$=1.8), thus resulting in spoon-shaped patterns (Fig. 5B).

Group 2 is characterised by REE pattern varying from slightly LREE-depleted to slightly enriched (Fig. 5D) and large variations in the MREE–HREE concentrations (e.g., CD 18 and CD 21, $La/Yb)_N$=0.8 and 0.5, respectively, and Nd to Yb concentration=~4 and ~2 x PM, respectively).

Group 3 clinopyroxenes have REE patterns varying from highly LREE-enriched and steadily fractionated [CD15, $(La/Yb)_N$=16.7] to moderately-LREE enriched and virtually flat from Gd to Yb (CD50 and CD28,

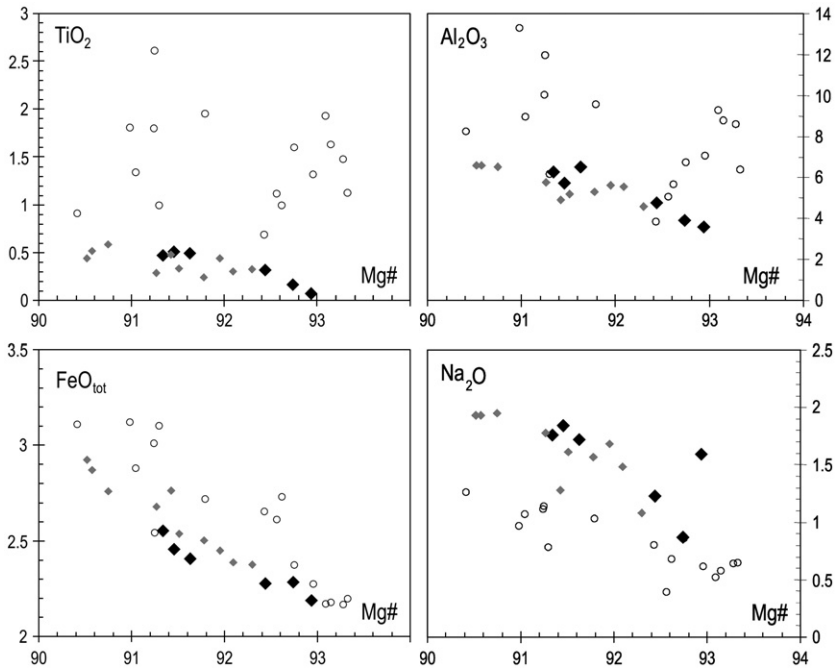

Fig. 4. Major element variation trends with respect to Mg# in the selected clinopyroxenes (black symbols) and in the larger data set from Rivalenti et al. (2004a) (grey symbols), compared with the clinopyroxenes crystallised in glass veins and pockets (open circles).

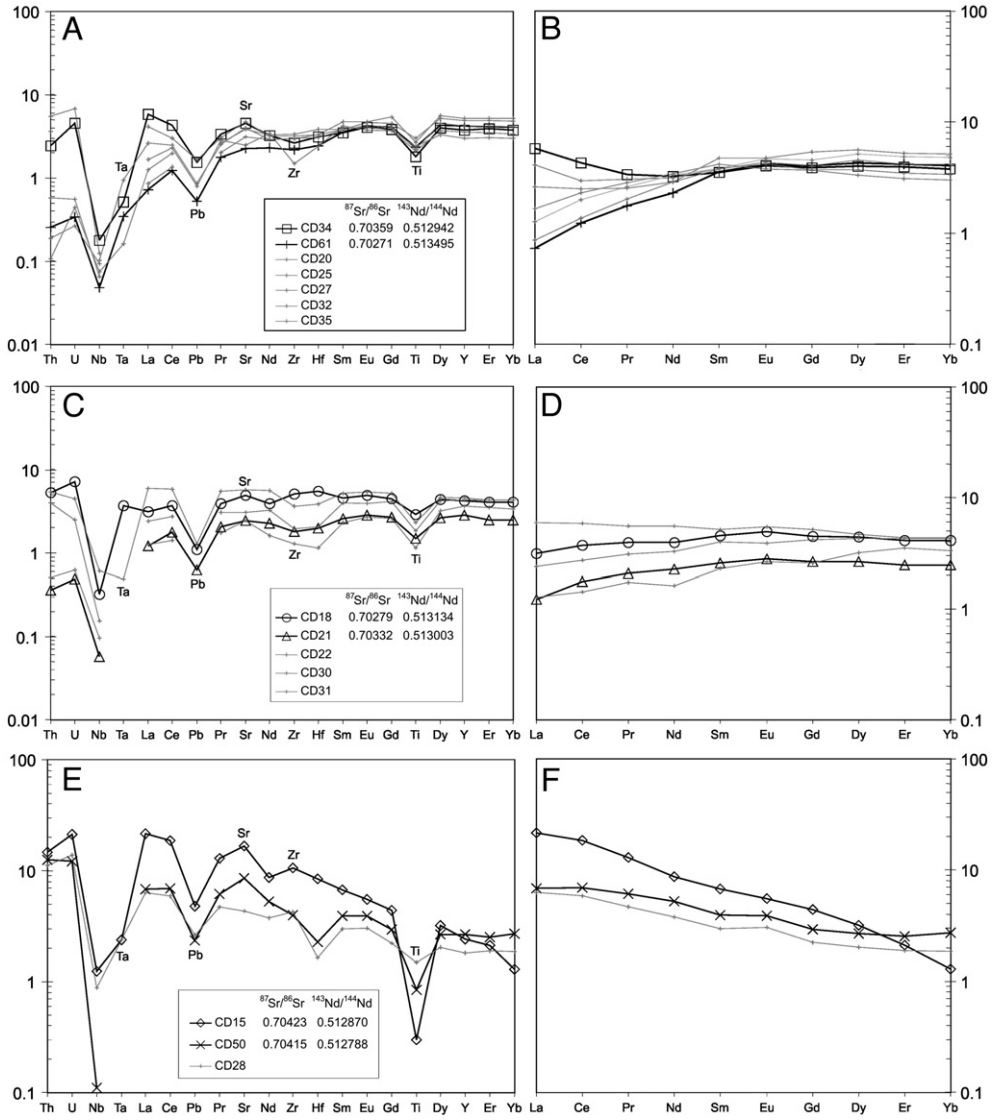

Fig. 5. Primitive mantle–normalised (Hofmann, 1988) REE and extended trace element profiles of the clinopyroxenes. Black lines and grey lines distinguish the clinopyroxenes selected for isotope analysis and the larger data set reported in Rivalenti et al. (2004a), respectively. Figs. A–B, C–D and E–F distinguish pyroxene groups with different geochemical characteristics discussed in the text.

$(La/Yb)_N = 2.5–3.4$ and $(Gd/Yb)_N = 1.1–1.2$, respectively) (Fig. 5F).

All groups have Th and U spikes (U being in general higher than Th), and negative Nb, Ta, Pb and Ti spikes. A positive Sr anomaly appears in all the clinopyroxenes except those LREE-depleted in the group 1. Concentrations of highly incompatible elements and Sr increase with increasing LREE concentrations. Zr and Hf do not show major anomalies in group 1 (they are slightly depleted with respect to the adjacent REE), and in group 2 Zr and Hf range from slightly depleted to slightly enriched. In group 3, Hf is markedly depleted in CD50 and both Zr and Hf are slightly enriched in CD15.

The Li and B concentrations are in the range 0.7–1.4 and 0.4–1.5 ppm, respectively lower and higher than those estimated by Ottolini et al. (2004) in the clinopyroxenes of the MORB mantle source (1.6–1.8 Li ppm and 0.07–0.10 B ppm). The clinopyroxenes having LREE-depleted patterns (CD61, CD21 and CD18) and high Mg# show the highest Li and lowest B concentrations. Li irregularly decreases, and B more regularly increases, with increasing the highly incompatible element concentrations and REE fractionation. Clinopyroxene CD34 is an exception due to its high Li content.

The variations of B and Li concentrations observed in the clinopyroxenes are matched by similar variations

in the other mineral phases (Table 1). B concentration does not show significant differences among the different mafic minerals, whereas Li is especially partitioned into olivine (e.g. Ottolini et al., 2004).

5.2. Sr and Nd isotopes

Analytical results on the clinopyroxene separates are reported in Table 2 and illustrated in Fig. 6. The samples form a tight array between a highly depleted DM end-member (the LREE-depleted *group 1* clinopyroxene CD61, $^{143}Nd/^{144}Nd = 0.51349$; $^{87}Sr/^{86}Sr = 0.70271$), and an enriched region occupied by the two *group 3* samples (the LREE-enriched clinopyroxenes CD15 and CD50, $^{143}Nd/^{144}Nd = 0.51287$, 0.51279; $^{87}Sr/^{86}Sr = 0.7042$, 0.7036, respectively). The isotopic variations correlate with those of the clinopyroxene geochemical parameters, as illustrated in Fig. 7 for selected elements. The increase in $^{87}Sr/^{86}Sr$ (or the decrease in $^{143}Nd/^{144}Nd$) correlates with the increase of the Mg# values and Sr, Zr, LREE, Pb, Th and B abundances and with the decrease of Na_2O, FeO, TiO_2, V, Y and HREE concentrations.

The Chenques isotope array is compared in Fig. 6 with other xenoliths from Patagonia, a large variety of Patagonia volcanics and Nazca plate basalts and sediments.

The isotopic values of the northern Patagonia xenoliths (Cerro del Mojon and Paso de los Indios, Barbieri et al., 1997) plot close to the Chenques array (Fig. 6A). The Cerro Fraile and Las Cumbres xenoliths, occurring in a region possibly affected by the Antarctic plate (Kilian and Stern, 2002), form an array that, starting from depleted values similar to those of Chenques, diverges towards a low-Nd, low-Sr end-member (Barbieri et al., 1999). The Pali Aike (not shown) and G. Gregores (Gorring and Kay, 2000) xenoliths behave like the backarc basalts. The Chenques samples are also compared in Fig. 6A with the isotopic characteristics of the xenoliths from Carpathian–Pannonian Basin (Rosenbaum et al., 1997), one of the few mantle wedge occurrences for which isotopic data are available. Like

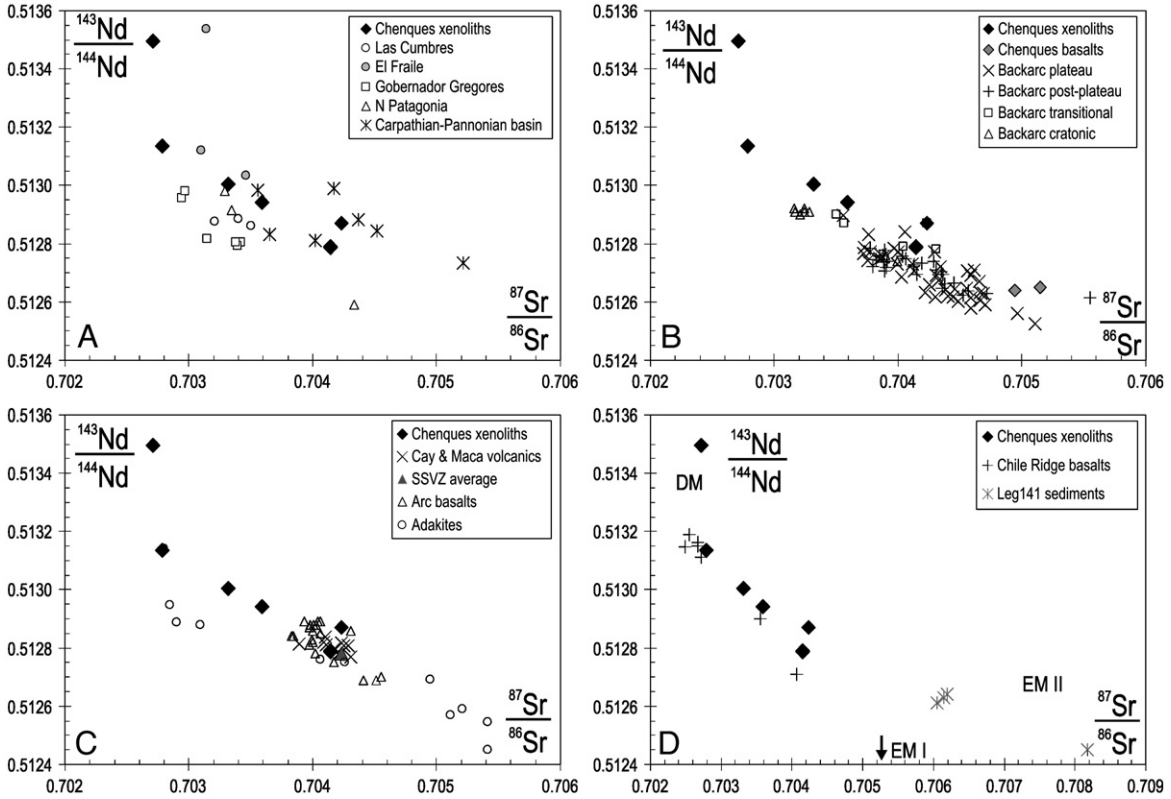

Fig. 6. Sr–Nd isotopic composition of the Chenques clinopyroxenes, compared with: A, other Patagonia xenolith occurrences (Northern Patagonia, Barbieri et al., 1997; Gobernador Gregores, Gorring and Kay, 2000; El Fraile and Las Cumbres, Barbieri et al., 1999) and xenoliths from Carpathian–Pannonian Basin (Rosenbaum et al., 1997); B, backarc plateau and post-plateau basalts (Stern et al., 1990; Gorring and Kay, 2001; Kay et al., 2007); C, arc basalts (Hickey et al., 1986; SSVZ: Kilian and Behrmann, 2003; Cay and Maca volcanoes: D'Orazio et al., 2003); adakites (Kay et al., 1993b; Stern and Kilian, 1996); D, Chile Ridge basalts (Klein and Karsten, 1995; Sturm et al., 1999) and Nazca sediments (Kilian and Behrmann, 2003)(D).

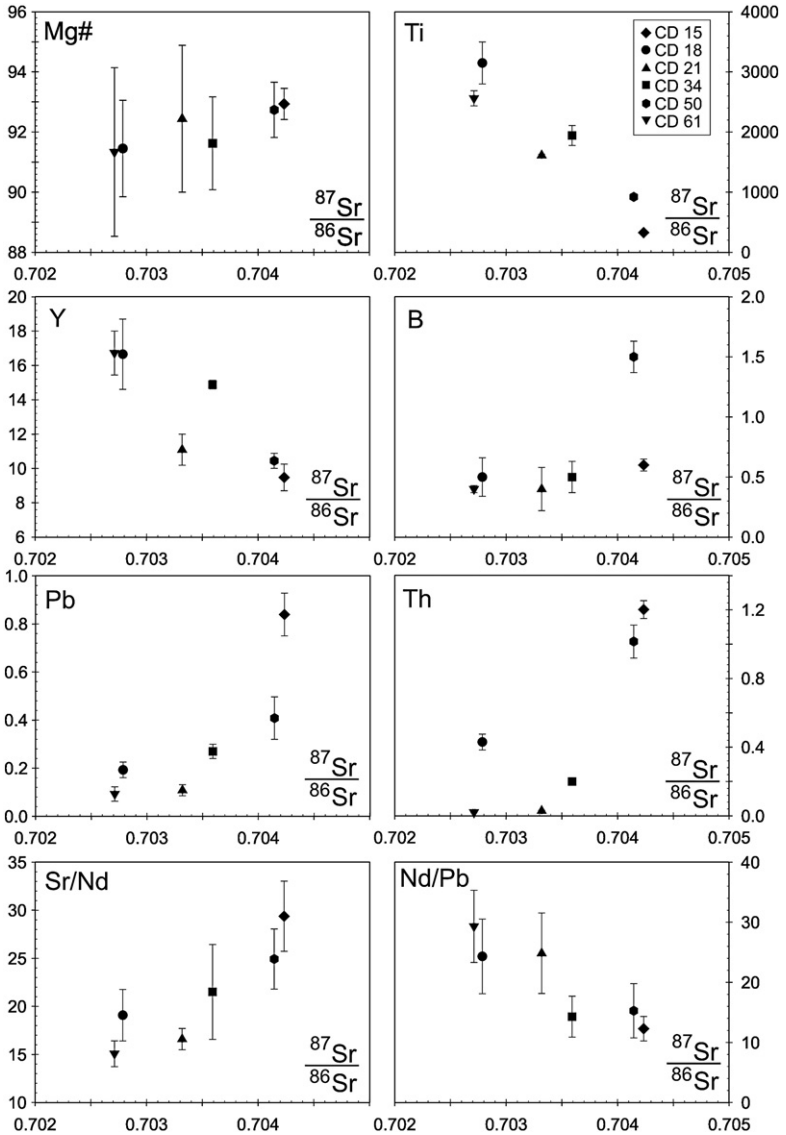

Fig. 7. Variation of selected trace elements (ppm) and element ratios with respect to $^{87}Sr/^{86}Sr$ in clinopyroxene. Bar represent 1σ standard deviation for the elements and element ratios, whereas standard deviation for the isotope is within the symbol dimension.

Chenques peridotites, the Pannonian xenoliths form an array enriched in radiogenic Sr.

The Chenques array is clearly distinct from that of the backarc lavas (Stern et al., 1990; Gorring and Kay, 2001; Kay et al., 2007) in being enriched in $^{87}Sr/^{86}Sr$ at a given $^{143}Nd/^{144}Nd$ (Fig. 6B). However, the alkali basalts of Chenques and another locality close to this (CH and PAT 4, respectively, Stern et al., 1990) plot in the proximity of the enriched end of the Chenques xenolith array.

The arc basalts from the SSVZ (Hickey et al., 1986; Kilian and Behrmann, 2003), especially those of two calc-alcaline volcanoes ~200 km SW of Chenques (Cay and Maca volcanoes, D'Orazio et al., 2003) and the adakites (Kay et al., 1993b; Stern and Kilian, 1996) partially overlap the Chenques array, extending it towards more enriched values (Fig. 6C). Some adakites from Cerro Pampa (Kay et al., 1993b), however, plot off the Chenques array at lower $^{143}Nd/^{144}Nd$.

Geochemical and isotope data on the Chile Ridge basalts and sediments forming the Nazca oceanic crust at the latitude of interest are from Klein and Karsten (1995), Sturm et al. (1999) and Kilian and Behrmann (2003). The Chile Ridge basalts have average $^{87}Sr/^{86}Sr$= 0.70296 and $^{143}Nd/^{144}Nd$=0.51305, with extreme Sr and Nd isotope values in one sample of Segment 4

(0.70407 and 0.512709, Klein and Karsten, 1995). The average $^{87}Sr/^{86}Sr$ and $^{143}Nd/^{144}Nd$ values in the sediments are 0.7077 and 0.51253, respectively (Kilian and Behrmann, 2003). The Chile Ridge basalts virtually overlap the Chenques xenolith array (Fig. 6D), whereas the Nazca sediments plot on the isotopically enriched extension of the Chenques array.

6. Discussion

As observed by Rivalenti et al. (2004a), the large variation in major and trace element compositions of the clinopyroxenes indicates that at Chenques the lithospheric mantle underwent metasomatic enrichment process. We discuss in the following the composition of the lithosphere predating metasomatism, the nature of the metasomatic agent(s) and their composition and origin.

6.1. Pristine lithosphere and metasomatic processes

Among the Chenques samples, CD61 and other geochemically similar samples not specifically considered in this paper (Fig. 5A,B) can be assumed as adequate representatives of the lithospheric mantle predating metasomatism. CD61 has the highest $^{143}Nd/^{144}Nd$ values resulting in a Proterozoic Nd model age and shares the geochemical characteristics typically considered to identify a Depleted Mantle (DM) reservoir (Hirschmann and Stolper, 1996), being in this respect similar to the pre-metasomatic mantle documented in other parts of the South America plate (.e.g., the xenoliths from NE Brazil; Rivalenti et al., 2007). It may be argued, however, that the secondary, re-crystallised textures characterising the DM Chenques xenoliths are unexpected in rocks recording very old mantle processes. Indeed, the only other Patagonian mantle xenoliths with a DM signature similar to CD61 occurs at Cerro del Fraile (sample Fr4, Barbieri et al., 1999) (Fig. 6A), but this sample has porphyroclastic textures. The presence of a secondary re-crystallised texture can be reconciled with DM characteristics only if the lithosphere underwent heating-induced re-crystallisation, without addition of exotic components; alternatively, the secondary re-crystallised texture could be ascribed to interaction with MORB-like melts having DM signatures. Since no Patagonia basalt has $^{143}Nd/^{144}Nd > 0.5130$, the second hypothesis is not favoured. Re-crystallisation induced by high temperature, on the other hand, agrees with the results of Kay (2002), who shows that the Patagonia mantle was close to melting since Mesozoic. Therefore, we assume that the pre-metasomatic lithosphere at Chenques had a DM composition and it underwent thermal re-crystallisation in relatively recent times.

The xenolith having the most isotopically enriched clinopyroxene, and consequently the highest concentration in highly incompatible trace elements, is harzburgite CD15. Both the strong depletion and fractionation of the moderately incompatible trace elements (e.g. HREE) suggest that the melt in equilibrium with clinopyroxene CD15 derived from a garnet-facies mantle sector. Therefore, the geochemical characteristics of this sample are assumed as the closest approach to the composition of the metasomatic agent. Correlations between isotopes and incompatible trace elements (Fig. 7) show that all the Chenques samples plot in between the CD61 and CD15 end-members and are, therefore, consistent with the effects of a metasomatic process by which a metasomatic agent (recorded by CD15) interacts with a lithosphere similar to CD61. The correlation between isotopes and fertility index, such as Mg#, indicates that the introduction of the metasomatic component was proportional to the degree of depletion in the ambient peridotite; in other words, either metasomatism affected a variably depleted mantle section, or the addition of the metasomatic component triggered melting so that the degree of this latter was roughly proportional to the amount of the metasomatic charge.

In group 1 clinopyroxenes, the metasomatic modifications, which affect only the most incompatible elements, result in spoon-shaped REE patterns like that of CD34 (but also CD20 and CD35 reported by Rivalenti et al., 2004a, Fig. 5B). In the region from Sm to Yb, the spoon-shaped patterns of group 1 clinopyroxenes are closely similar to pattern of CD61 clinopyroxene. This is consistent with metasomatic processes operated in a lithosphere having geochemical signatures similar to those of CD61. The high concentration of the LREE, as well as of other LILE, in the spoon-shaped clinopyroxenes may be regarded as the result of melt percolation through the fertile lithospheric peridotites at a given stage, namely when the melt is progressively exhausted by fractional crystallisation and its composition is strongly affected by chromatographic-type chemical exchange with the peridotite. At this stage, the composition of moderately incompatible trace elements (e.g. HREE) in the percolating melt is efficiently buffered to that of peridotite minerals, whereas the highly incompatible elements still have variably large contents and are ubiquitously strongly fractionated (see also Xu et al., 1998; Ionov et al., 2002; Rivalenti et al., 2007).

In the group 2 samples, and in samples CD50 and CD28 from group 3, large variations in REE concentrations are associated with only slight REE fractionation

and depletion in modal clinopyroxene. In other occurrences, similar features have been interpreted and modelled as the transient result of melt-peridotite reactions dominated by dissolution of peridotite minerals and consequent increase of the melt volumes (Bedini et al., 1997; Xu et al., 1998). The chemical effects of this process are closely similar to those produced by melt-assisted partial melting (e.g., Rivalenti et al., 2007); its occurrence and relevance in the evolution of the Southern Patagonian lithosphere has been already addressed elsewhere (Rivalenti et al., 2004a,b).

Metasomatic processes resulting in chromatographic enrichment are commonly described and quantitatively modelled in several studies (e.g. Kelemen, 1995; Bedini et al., 1997; Rivalenti et al., 2007). Using the Plate Model of Vernières et al. (1997), we provide here (Fig. 8) a numerical simulation of the melt-assisted partial melting recorded by the group 2 and 3 xenoliths and of the chromatographic enrichment in the group 1 xenoliths.

The melt in equilibrium with clinopyroxene CD15 has been assumed to represent the infiltrating melt, whereas the trace element composition of the pristine mantle has been inferred by mass balance calculations using the CD61 mode, clinopyroxene composition and solid-solid trace element partitioning derived from suitable solid-melt partition coefficients (Ionov et al., 2002). Reaction parameters were progressively refined to verify the possibility that the chemical signatures of melt in equilibrium with the CD50 clinopyroxene are a transient feature produced by melt-peridotite interaction under increasing melt mass conditions. The mantle column was divided in 20 cells and 20 process increments were run; peridotite minerals were assumed to dissolve during each increment in the following weight fraction Opx:Cpx:Sp=0.2:0.7:0.1, according to the petrographic observation. This is also consistent with the minerals weight fraction of peridotite melting assemblage at spinel facies conditions (Kinzler, 1997). The starting melt/rock ratio was fixed to 0.01. Fractional crystallisation was not allowed, whereas an assimilation rate of peridotite minerals was set to 7 per mill throughout the column. Compaction was carried out in cells with melt/rock values exceeding 0.03. For a detailed explanation of model parameters see Vernières et al. (1997). After 20 process increments, the melt/rock mass ratio was 0.03, with the exception of the last two cells, in which it was between 2.5 and 1.7. The upper part of the mantle column maintains a lherzolite composition. The last cell atop the column, which experienced only 1 process increment, has the following mineral assemblage (weight fraction): Ol:Opx:Cpx:Sp=0.605:0.260:0.116:0.019. This assemblage is, in practise, indistinguishable from the original modal composition, whereas it becomes progressively more olivine-rich towards the bottom of the reaction column. The first cell at the base of the column has a harzburgitic modal composition with Ol:Opx:Cpx:Sp=0.690:0.269:0.033:0.008 (weight fraction). Other model parameters are reported in the caption of Fig. 8. This Figure shows the trace-element abundances in clinopyroxenes CD61, CD15, CD50 and CD34 (black lines) and the model clinopyroxenes (grey lines) of the first 5 cells and 10th, 15th and 20th cell.

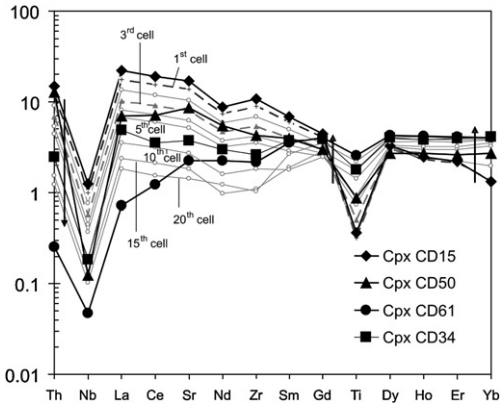

Fig. 8. Numerical simulation (Plate Model, Vernières et al., 1997) of reactive porous flow of a putative melt in equilibrium with clinopyroxene CD15 through a fertile spinel-facies lithospheric mantle containing clinopyroxene CD61. The Fig. shows the PM-normalised trace-element abundances in clinopyroxenes CD61, CD15, CD50 and CD34 (black lines) and the model clinopyroxenes (grey lines) of the first 5 cells and 10th, 15th and 20th cell. The clinopyroxene/melt partition coefficients used in the model are from Green et al. (2000, run 1802). The solid/melt partition coefficients for olivine are from Zanetti et al. (2004), whereas those for orthopyroxene and spinel were calculated according to the Cpx/liquid partition coefficients of Green et al. (2000) and the solid/liquid partition coefficients reported by Ionov et al. (2002). See text for further explanations.

The results of our modelling show that the concentration of highly incompatible trace elements in the metasomatic fluid triggering melting (and consequently, in the equilibrium clinopyroxene) decrease as the reaction with ambient peridotite proceeds; however, only moderate changes among highly incompatible trace elements are observed. By contrast, the concentrations of moderately incompatible elements in the metasomatic melt increase with significant changes of the original fractionation. The REE, Sr, Zr, Ti and Y contents of clinopyroxene CD50 are best modelled at the base of the mantle column, where the peridotite is deeply modified (i.e. modally depleted and enriched in incompatible elements) by interaction with the upraising melt. The mismatch observed in Th and LREE fractionation

between the compositions of CD50 and modelled clinopyroxene does not likely result from melt-peridotite interaction and, it is, therefore, regarded as due to the original compositional features of the injected fluid coming from garnet-facies reservoir. Spoon-shaped trace element patterns similar to those observed in the group 1 xenoliths (e.g. CD34) are approximated in the 10th to 20th cells.

As a whole, melt-assisted melting results in more refractory (harzburgitic) assemblages with enriched trace element signatures at the bottom of the column, and more fertile or almost primitive (lherzolitic) assemblages with slightly modified trace element signatures towards the top of the mantle column.

6.2. Nature of the metasomatic agent

The isotopic signatures of Chenques xenoliths provide evidence in favour of a slab-derived signature of the metasomatic agent beneath this locality. As a whole, the observed isotopic array has close similarities with that of arc lavas (especially Cay and Maca) and adakites from the region (Fig. 6C), both containing important contributions from the subducted slab, and points to an enriched end-member, possibly represented by a mixture of Nazca basalts and sediments. Similarly, the radiogenic-Sr-enriched trend shown by ultramafic xenoliths from the mantle wedge of the Carpathian–Pannonian Basin (Rosenbaum et al., 1997) (Fig. 6A) was attributed to the interaction of peridotite mantle with liquid(s)/melt(s) carrying a relatively large amount of slab-derived component(s).

The initial geochemical characteristics of the metasomatic agent are best recorded in the CD15 sample from group 3 xenoliths (see discussion in Section 6.1), whereas all the other samples record either melting triggered by the metasomatic agent (CD50 and group 2 xenoliths) or the results of chromatographic element fractionation (group 1). In order to make easy the comparison between possible metasomatic agents and the potential melts in equilibrium with clinopyroxenes, we calculated the composition of these latter by using the partition coefficients of Green et al. (2000, run 1802, at 1080 °C and 2 GPa)

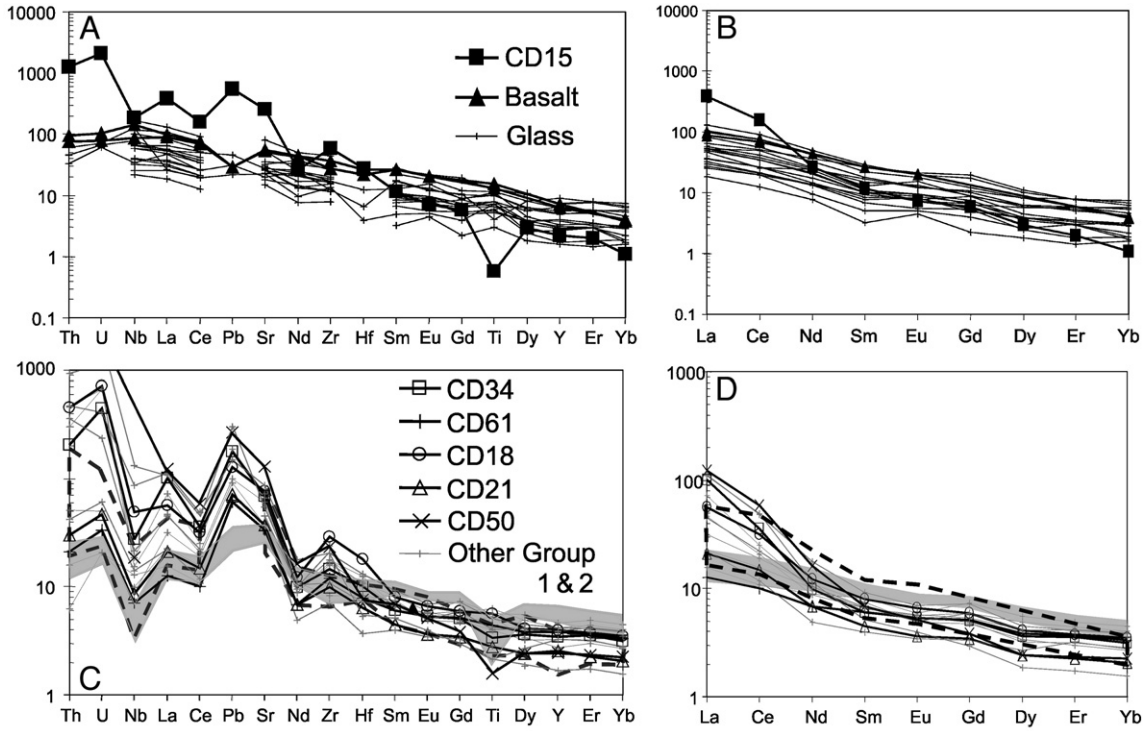

Fig. 9. A, B: PM – normalised extended and REE patterns of the melt in equilibrium with the matrix CD15 clinopyroxene compared with the host alkali basalt and with the glass composition in veins and pockets into the xenoliths. C, D: melts in equilibrium with the group 1 and 2 clinopyroxenes specifically studied in this paper and from literature (Rivalenti et al., 2004a) compared with the Cay and Maca basalts (field contoured by dashed lines, D'Orazio et al., 2003) and the field of the Patagonia adakites (in grey, Kay et al., 1993b; Stern and Kilian, 1996). Equilibrium melts were calculated by using the partition data set of Green et al. (2000) for hydrous basalt at 2 GPa and 1080 °C (corresponding with the temperature range of the xenoliths and their spinel-facies) and of Hauri et al. (1994) for Th, U and Pb.

and of Hauri et al. (1994) for Th, U and Pb at 1407 °C and 1.7 GPa. In spite of the large temperature differences, the two runs have similar $^{cpx/l}D_{La,Ce}$.

The CD15 equilibrium melt (Fig. 9A, B) exhibits positive Th, U, Pb and Sr spikes, negative Nb and Ti spikes and highly fractionated REE pattern indicating derivation from a garnet-bearing source. The LILE enrichment and the negative Nb spike are preserved during the melting-assisted process described in Section 6.1, except for a decrease of the REE fractionation produced by the re-equilibration with the spinel-facies mantle. These geochemical characteristics are generally considered as typical of components bearing a subduction-related signature (e.g. Ionov and Hofmann, 1995; Kepezhiskas et al., 1996; Yagodzinski and Kelemen, 1998; Dorendorf et al., 2000; Churikova et al., 2001; Grégoire et al., 2001; Prouteau et al., 2001; Franz et al., 2002; Trua et al., 2006).

Metasomatism operated by an alkali basalt component is an alternative possibility to the model depicted above, namely the straightforward interaction of peridotite mantle beneath Chenques with a fluid containing a slab signatures. Numerical simulations provided in the last decade (Vernières et al., 1997; Bedini et al., 1997; Ionov et al., 2002; Rivalenti et al., 2004b, 2007; Piccardo et al., 2007) demonstrated that percolating melts may significantly change their initial composition during reactive porous-flow. Low time-integrated melt/rock mass ratios may result in extreme incompatible element enrichment and inter-element fractionation, particularly in the presence of trace-element-bearing accessory minerals. For example, Bedini et al. (1997) attributed the enrichment in LILE and LREE and the depletion in Nb and Ta observed in xenoliths from the East African rift to the percolation of alkali-basalts under decreasing melt mass and the concomitant crystallisation of microphases (e.g. rutile). Similarly, Ti, Zr and Hf negative anomalies of clinopyroxenes from Gobernador Gregores xenoliths were not ascribed to metasomatism operated by an agent strongly depleted in HFSE, such as a carbonatitic melt, but to the role of HFSE-bearing phases such as amphibole and loveringite during reactive porous flow operated by hydrous alkaline basalts (Rivalenti et al., 2004b).

In the specific Chenques case, isotopic signatures (Fig. 6B) clearly indicate that the only backarc alkali basalt suitable to have metasomatised the Chenques lithosphere is the basalt hosting the xenoliths. Insights on the chemical variations induced by percolation of the host basalt into the CD mantle are provided by the occurrence of vein glasses. Preliminary results bear evidence for strong reaction between the infiltrating host lava and the matrix mineral assemblage, resulting in orthopyroxene dissolution and crystallisation of olivine, clinopyroxene, spinel±plagioclase. As a result, the lava undergoes dramatic chemical variations consisting, at the thin section scale, of silica, aluminium, alkalis and Mg# increase recorded by vein glass (see representative glass analyses in Table 1, supplementary material). These variations are similar to those described by Shaw et al. (2006). The trace element patterns available at present (Fig. 8) show that, in spite of the large major element variations, the infiltration process does not induce any trace element fractionation; spikes in Th, U, Nb, Pb, Sr and Ti, such as those observed in equilibrium melt of CD15 or in any other melt estimated from the xenolith clinopyroxenes, are not observed. Significant differences also exist between the major element composition of matrix clinopyroxenes and those crystallised from vein glass (representative analyses in Table 1, supplementary material) within the same Mg# range (Fig. 4). It is therefore concluded that there is no evidence in favour of the host basalt as the metasomatic agent. Arc basalts, adakites or even slab-derived liquids are better candidates as potential metasomatic agent, as suggested by their similarity with melts in equilibrium with clinopyroxene (Fig. 9C and D). The main difference between the equilibrium melts and the arc magmas is the higher concentration of the incompatible elements in the range Th–Pb in the melts, possibly caused by the chromatographic enrichment of these elements in the infiltrating agent during metasomatism.

6.3. Site of metasomatism

It has been shown in Section 6.2 that the Chenques xenoliths bear isotopic and geochemical evidence of their interaction with components derived from the subducted plate. However, the Chenques locality occurs 200 km E from the SSVZ, that is very far from the location we could expect for extensive interaction of sub-arc mantle with slab-derived components. Therefore, either the Chenques xenoliths represent subarc mantle transported 200 km to the E, or they record a metasomatic event operated beneath the Chenques occurrence by slab-derived components. These two possibilities are discussed in the following.

6.3.1. Subarc mantle

The hypothesis that the Chenques xenoliths derive from the subarc mantle of the SSVZ requires reverse corner flow in the mantle wedge. Davies and Stevenson (1992) extensively discuss the factors inducing reverse

in the corner flow (e.g. buoyancy, presence of a week layer, presence of subducted sediments). These requirements could be matched by the SSVZ subarc mantle. However, the SSVZ volcanoes range in age from Pliocene to Quaternary. Thus, assuming an age of ~5 Ma, the velocity of the flow had to be ~4 cm year^{-1} in order to travel the 200 km separating the Chenques locality from the arc. van Keken (2003) highlights the several factors controlling the flow velocity in the wedge corner. These factors are unknown in the present case and thus it is impossible to constrain the velocity. Although attractive, this scenario is probably not reasonable because of the lack of deformed textures in the collected xenoliths (Fig. 3), which do not favour solid-state transport over long distances but, rather, *in situ* recrystallisation.

6.3.2. Metasomatism beneath the Chenques locality

If unrelated to the upraise of the Quaternary host basalts, the age of metasomatism is essentially unconstrained because subduction was active since Mesozoic (Ramos and Aleman, 2000). However, the secondary nature of petrographic textures suggests that the chemical heterogeneity of the Chenques samples can be broadly considered coeval with the Tertiary-Quaternary stages of backarc magmatism. If metasomatism is older than 14 Ma, the triple point (Fig. 1) would have been at latitude 50° S (Ramos and Kay, 1992; Gorring et al., 1997; Ramos and Aleman, 2000) and at the Chenques latitude subduction would have involved colder regions of the Nazca plate with respect to present because farther from the Chile Ridge. In the following discussion we postulate that the subduction geometry and the plates involved were similar to those involved at present.

Spinel-facies xenoliths come from a depth not exceeding 60–70 km. Because the Chenques locality is 400 km far from the Chile trench, the slab surface under this locality must have reached a depth around 180 km, even assuming a moderate slab dip of about 20° (Cahill and Isaks, 1992). This depth estimate is consistent with the geophysical data of Gutscher (2002) at latitude 42° S. If so, slab-derived component was released to the wedge at pressure >5 GPa and had to cross a ~100 km thick, hidden mantle section before reaching the spinel-facies level. Among the many factors controlling the observed metasomatism (temperature of the subducted slab, its mineralogical and chemical variation at increasing depth, composition of the released fluids, reactions occurred during percolation in the garnet-facies mantle), only the composition of the Nazca plate sediments and basalts before subduction and the final metasomatic overprint is known. However, based on available experimental work, we propose three main cases for the processes occurring in the hidden region. These hypotheses are illustrated in the cartoon in Fig. 10 and discussed in the following.

6.3.2.1. Slab components are released as hydrous fluids and not melts and reactions in the major dehydration zone beneath the arc do not consume all water. The main dehydration zone beneath the arc involves the breakdown of amphibole, biotite and other hydrous phases like lawsonite and zoisite (Schmidt and Poli, 1998; Hermann and Green, 2001; Forneris and Holloway, 2003). According to Poli and Schmidt (1995), Hermann and Green (2001) and Schmidt et al. (2004) the main water carrier at higher pressures is phengite both in basaltic and metasedimentary components, which would be composed by garnet+clinopyroxene+phengite±kyanite±rutile. As shown in Table 3, both the Nazca sediments and basalts may be calculated according to a high pressure mode containing phengite.

An important requirement is that the slab preserved subduction-related trace element signature downstream the main dehydration zone. This may happen only if the slab components released beneath the arc were fluids and not melts, since melts would deplete the residual slab in incompatible trace elements much more efficiently than fluids. If older than 15 Ma, the subducted Nazca plate in the region of interest may have been relatively cold and, at a convergence rate high as at present, it may have not been heated to the melting temperature (>750 °C at ~3 GPa) below the arc (Forneris and Holloway, 2003). Relatively cold slab is supported by the conclusions of D'Orazio et al. (2003), who claim that the mantle source of the Cay and Maca arc volcanics was fertilised by slab fluids and not melts.

6.3.2.2. Mobile slab components are released as supercritical fluids beneath Chenques. Schmidt et al. (2004) show that in phengite-bearing metabasalts and metasediments melting may occur under fluid saturated conditions at ~850 °C, 4 GPa, being melt productivity proportional to the phengite content. The experimental melt is a high-K granite (Table 3 in Schmidt et al., 2004) enriched, besides K, in Rb and Ba because phengite is the main carrier for these elements. Stalder et al. (2001) show that with increasing pressure the amount of dissolved matter in a fluid and of water in the melt dramatically increase and the compositions of fluids and melt converge along a miscibility gap that eventually disappears. Any fluid beyond the intersection of the miscibility gap with the solidus is a "supercritical liquid" indistinguishable from melt. According to Kessel et al.

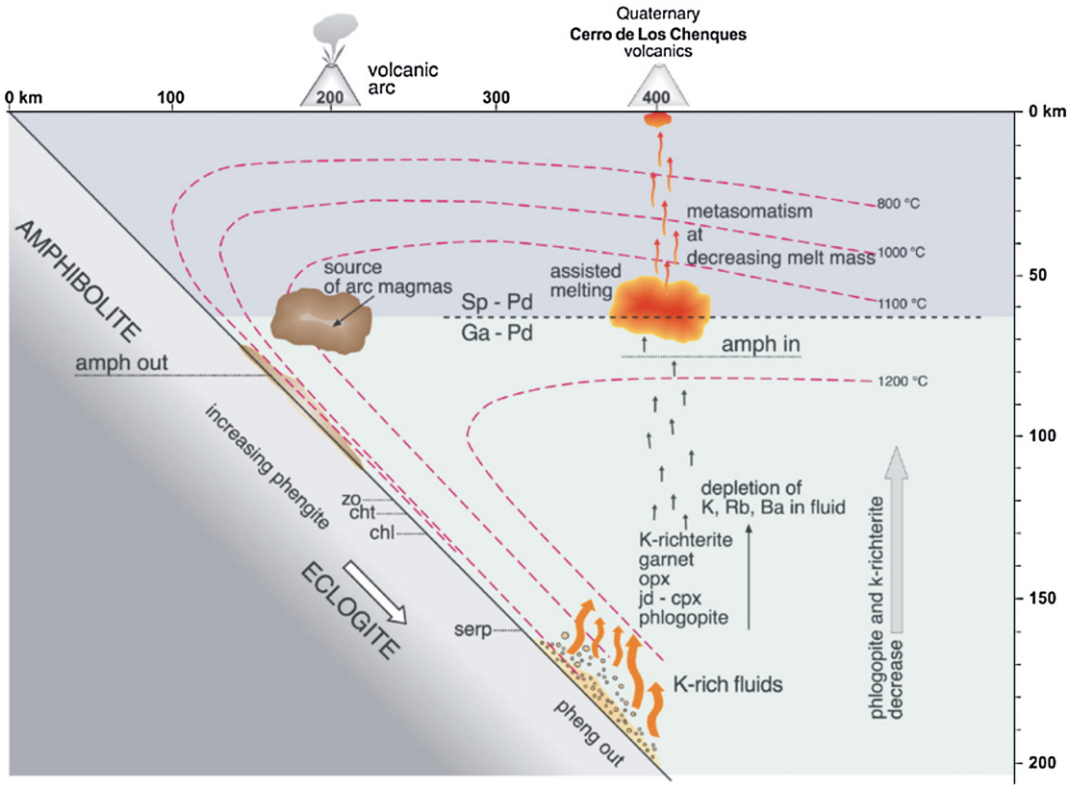

Fig. 10. Cartoon illustrating the hypothesis that the Chenques metasomatic agent derives from the underlaying slab and refers to pre-Qaternary processes. The figure shows the upper stability limit of hydrous phases along the subducted slab (from Schmidt and Poli, 1998), and summarizes the fertilization effects induced by fluid percolating in the garnet-facies mantle wedge and the metasomatic processes occurring in the spinel-facies mantle. Depth and distance from the trench are not at the same scale. A subduction dip of ~20° has been assumed. Isotherms are only indicative. Amph = amphibole; zo = zoisite; cht = chloritoid; chl = chlorite; serp = serpentine; pheng = phengite; Sp = spinel; ga = garnet.

(2005), this critical end-point is situated between 5 and 6 GPa in mica-rich lithologies and Schmidt et al. (2004) propose termination of the wet solidus slightly above 5 GPa. This fluid is water-rich and enriched in K and all the elements partitioned into phengite; moreover, it possess highly fractionated REE patterns and is depleted in Ti and Nb because of the presence garnet and rutile in the residual eclogite.

It is here postulated that slab temperature was not sufficiently high to induce phengite-controlled melting beneath the Chenques areas and that phengite breakdown (at about 6 GPa) resulted in a supercritical fluid.

Kessel et al. (2005) provide fluid/eclogite partition coefficients at 4 and 6 GPa and at various temperatures. These partition coefficients account also for the presence of rutile. Although the experimental charges were K-free, Kessel et al. (2005) claim that the partition coefficients may be applied also to K-rich pelitic and clastic metasediments. At 6 GPa, partition coefficients between supercritical fluids and solids show a large T-dependence, but are qualitatively similar to solid/melt D values.

Putative trace element abundances of supercritical fluids, estimated from the Nazca metasediments and metabasalts, using the solid/liquid partition coefficients defined by Kessel et al. (2005) at 6 GPa and various temperatures, assuming fluid extraction up to the complete disappearance of phengite, are reported in Table 3. Both sediment- and basalt-derived fluids show T-related variations of both the overall element concentrations and elemental fractionation, especially regarding Th/U, La/Nb, (Zr,Hf)/Nd, whereas REE fractionation remains virtually unchanged.

6.3.2.3. Supercritical fluids survive flow into the hidden mantle segment. First, let consider the ability of a slab-derived fluid to travel the long distance to the spinel-facies level. We speculate that this occurred for two reasons: a) the inverted geothermal gradient of the wedge; b) the preservation of H_2O in the fluid. Because of the inverted

Table 3
Average of the Nazca Plate Leg 141 sediments and Chile Ridge basalts and estimated fluid compositions at 6 GPa

	Leg 141 Sediment [a]					Chile Ridge basalts [b]				
	Average	FLUIDS at 6 GPa [c]				Average	FLUIDS at 6 GPa [c]			
		800 °C	900 °C	1000 °C	1200 °C		800 °C	900 °C	1000 °C	1200 °C
SiO_2	58.27					50.00				
TiO_2	0.91					1.22				
Al_2O_3	16.27					15.60				
FeO	7.02					8.98				
MnO	0.11					0.17				
MgO	3.01					8.50				
CaO	4.48					11.50				
Na_2O	3.44					2.70				
K_2O	2.12					0.19				
P_2O_5						0.14				
Total	95.62					99.00				
Ti	5428	727	1626	7178	10906	7322	748	1753	10948	23051
Sr	295	949	957	1002	1012	136	2112	2248	3248	3586
Y	23.9	1.4	1.7	10.7	28.3	29.4	1.3	1.6	11.1	37.4
Zr	149.5	19.6	68.4	288.1	394.3	94.0	9.4	36.0	271.4	601.0
Nb	9.1	3.9	10.4	16.6	25.4	3.7	1.3	4.5	9.7	29.5
Ba	442	1469	1490	1526	1522	51	1004	1131	1434	1400
La	21.6	62.5	66.1	73.0	74.5	4.3	39.3	50.9	100.5	124.7
Ce	47.6	124.4	137.4	155.4	163.8	11.4	70.8	102.1	199.0	316.4
Nd	22.8	34.5	44.1	70.7	72.8	9.3	17.3	27.1	117.4	138.5
Sm	4.92	3.61	4.61	10.33	12.67	3.02	2.02	2.76	10.46	17.83
Eu	1.21	0.61	0.82	1.91	2.61	1.07	0.46	0.65	2.13	3.94
Gd	4.54	1.26	1.97	4.62	7.32	4.07	0.90	1.47	4.17	8.42
Dy	4.09	0.35	0.53	1.54	3.15	4.82	0.31	0.48	1.48	3.43
Er	2.42	0.10	0.13	0.45	1.08	2.91	0.09	0.12	0.42	1.09
Yb	2.19	0.06	0.06	0.27	0.71	2.88	0.06	0.06	0.27	0.75
Hf	2.21	0.37	1.20	4.61	6.00	2.22	0.29	1.04	7.59	15.67
Ta	0.641	0.147	0.513	1.076	1.770	0.230	0.041	0.172	0.510	1.727
Pb	13.37	42.47	42.56	44.36	45.68	0.64	9.22	9.35	12.52	16.34
Th	7.00	17.06	22.19	23.51	24.21	0.52	2.62	7.47	11.37	15.30
U	1.89	3.01	4.17	6.02	6.52	0.13	0.27	0.51	1.91	3.67
143Nd/144Nd	0.512530					0.513054				
87Sr/86Sr	0.707700					0.702961				
High pressure mode [d]										
Pheng	28.6					2.9				
Gar	11.0					4.5				
Cpx	32.1					79.9				
Coes	19.1									
Ky	8.1					11.9				
Ru	1.0					0.9				
R2	2.5					2.0				

Cl = Co/(F+D*(1-F)), assuming F = phengite percent in sediments and Chile ridge basalts. R2 = S of square residuals.
[a] Leg 141 sediments: Kilian and Behrmann (2003).
[b] Chile Ridge basalts: Klein and Karsten (1995), Sturm et al. (1999).
[c] Calculated by mass balance using the phase compositions of sample 1912 from Green and Adam (2003, Eur J. Mineral. p.821).
[d] Fluid composition estimated from the fluid/eclogite partition coefficients from Kessel et al. (2005) and batch melting equation.

geothermal gradient, the fluids would be heated while migrating, so decreasing their viscosity. Another factor decreasing the viscosity is the decrease of silica content related to the olivine-dissolving and orthopyroxene-forming reactions. As for *b*, because of the K-rich and hydrous composition of the slab-derived component, phlogopite and amphibole are likely to be reaction products. In the absence of a vapour phase, amphibole is stable up to 1150 °C and 3 GPa and phlogopite up to 1250 °C at 5-6 GPa (Sudo and Tatsumi, 1990; Wallace and Green, 1991; Niida and Green, 1999). Therefore, phlogopite is the dominant hydrous phase crystallising in

garnet-facies mantle and amphibole may appear at the garnet-spinel-facies transition (Fig. 10). Hermann and Green (2001) demonstrate that the H_2O/K_2O ratio of the slab-derived melt is much higher than that of phlogopite and amphibole, which are, therefore, not adequate to store the whole H_2O content of the hydrous fluid or melt. This is also re-enforced by the results of Hauri et al. (2006), who show that in mantle systems water is incompatible both in mica and amphibole.

Crystallisation of phlogopite depletes the infiltrated melt in Rb, K, Ba; all other elements are mostly unaffected due to the very low partition coefficients between phlogopite and melt (Green et al., 2000). Noticeably, Rb removal during phlogopite crystallisation results in "freezing" the $^{87}Sr/^{86}Sr$ of the fluid (Schmidt et al., 1999).

In mantle amphibole, Ti is compatible and Nb may become compatible in high-silica, dehydrogenated amphiboles (Tiepolo et al., 2000a). Partitioning of REE between amphibole and melt is essentially similar to that of the coexisting clinopyroxene, although at slightly higher D values (LaTourrette et al., 1995; Tiepolo et al., 2000b). Amphibole may, however, induce MREE fractionation with respect to LREE and HREE; Tiepolo et al. (2000b) show that amphibole $^{amph/melt}D_{Nd\text{-}Dy}$ may become compatible when $^{amph/melt}D_{LREE}$ and $^{amph/melt}D_{Er,Yb}$ are still incompatible. As reviewed in Rivalenti et al. (2004b), amphibole may also induce variations in inter-element HFSE fractionation, but it is unlike to change the REE-HFSE fractionation.

Since the slab-derived fluid was initially in equilibrium with a garnet- and clinopyroxene-bearing residuum, its re-equilibration with these phases may result in negligible percolation-related geochemical variations; however, this process may have increased the Mg# number of the fluid and the jadeite content of clinopyroxene (Yaxley and Green, 1998). Salters et al. (2002) show that Pb is more incompatible than Ce in clinopyroxene and, according to Green et al. (2000) Sr is more incompatible than Ce and Nd in garnet. According to Salters et al. (2002), D_{HREE} between garnet and melt decrease at increasing pressure, U is less incompatible than Th and Hf less incompatible than Zr (see also van Westrenen et al., 2001).

6.3.3. Comparing the CD15 equilibrium melt and fluids reaching the spinel-facies mantle

An indirect estimate of the chemical variations experienced by the slab fluids during their percolation into the hidden mantle can be done by comparing the geochemical characteristics of the initial fluid with those of the melt in equilibrium with the CD15 clinopyroxene, which was assumed as representative of the metasomatic agent reaching the spinel-facies mantle. A mixture of 60% sediment – and 40% basalt-derived fluids at 6 GPa and 1000 °C has been chosen as representative of the initial fluid. These relative proportions have been chosen to roughly account for the isotopic values of the enriched end-member of the Chenques isotopic array ($^{87}Sr/^{86}Sr=0.70446$; $^{143}Nd/^{144}Nd=0.512805$). Fig. 11 shows that the trace element pattern for CD15 potential melt is qualitatively similar to the high temperature (>1000 °C) fluid mixture for the highly fractionated REE patterns, positive Th, U, Pb, Sr and negative Nb anomalies. However the CD15 melt has a slightly downward-convex REE pattern, which is slightly upward-convex in the fluids, thus resulting in higher $(La/Sm)_N$ and lower $(Sm/Yb)_N$ of the first one. The CD15 melt is also enriched in Th, U, Nb, Pb, Sr and depleted in Ti with respect to the fluids. Based on the effects of percolation into the hidden mantle zone described above, the differences in the REE pattern may be a consequence of amphibole crystallisation. The

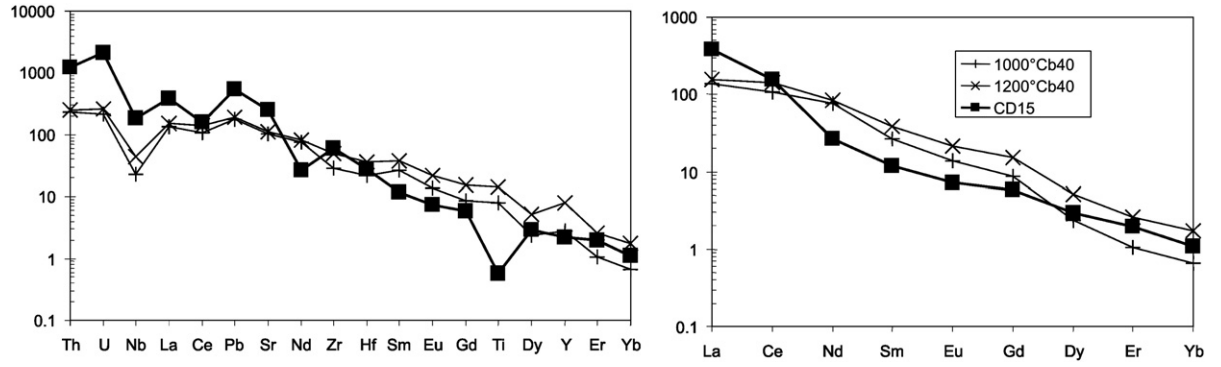

Fig. 11. Comparison of the potential CD15 equilibrium melt with a 60% metasediment–40% basalt-derived fluid mixture (b40 in the figure) estimated by using the high pressure mode of Nazca sediments and basalts, their average composition and the partition coefficients of Kessel et al. (2005) at 6 GPa and 1000–1200 °C (Table 3).

higher concentrations of Pb and Sr are consistent with the higher incompatibility of these elements in clinopyroxene and garnet with respect to Ce, thus becoming relatively enriched during fluid percolation at decreasing fluid/rock ratio. This may also be the case for Th and U. The higher Ti depletion in the CD15 melt can be regarded as a consequence of amphibole fractionation. This is also consistent with the differences observed for Nb, whose concentration is higher in the CD15 melt, whereas the La/Nb ratio is lower, suggesting that Nb was incompatible in amphibole, but less incompatible than La and Ce. Zr enrichment with respect to Hf and to adjacent REE may reflect a garnet influence.

6.4. B and Li

Since B and Li concentration are unknown in the Nazca sediments and basalts, we did not modelled their variation determined by the subduction process. These elements are known to be relatively concentrated in altered oceanic crust (e.g. Seyfried et al., 1983). Although Chenques pyroxenes and other phases have relatively high concentrations of B and Li, they are less enriched than LREE. In the models previously discussed, this may be explained by two causes: a) the slab beneath Chenques underwent B and Li removal when passing underneath the volcanic arc; b) B and Li have lower fluid/solid partition coefficients than LREE. As for point a, B and Li decrease at increasing slab dehydration is consistent with the conclusions of Brenan et al. (1998a,b). A decrease of B and Li concentrations with increasing slab depth is reported by Scambelluri et al. (2004). As for point b, fluid/solid partition coefficient at 6 GPa reported by Kessel et al. (2005) indicate much higher $^{fluid/solid}D_{La,Ce}$ (17.6–206 and 11.8–159, respectively, in the range 900–1200 °C) than for $^{fluid/solid}D_{B,Li}$ (11.5–7 and 1.52–7.2 in the same temperature range).

Comparison of the present data with those reported in the $(Li/Yb)_{cpx}$–$(Ce/B)_{cpx}$ diagram of Ottolini et al. (2004) shows that the Chenques pyroxenes have lower Ce/B values than the subcontinental mantle values, which may indicate influence of fluids. In the literature, data on the Li and B concentration in clinopyroxenes of supra-subduction mantle wedge are, to our knowledge, lacking. So, if our models are reliable, the present data set is an important information about clinopyroxene composition in this geodynamic environment.

7. Conclusions

Clinopyroxene geochemistry and its estimated equilibrium melts indicate that at Chenques the spinel-facies mantle was a slightly depleted lherzolite which partially melted during the introduction of a metasomatic component or was only chromatographically enriched in highly incompatible elements in those sectors where metasomatism occurred under decreasing melt mass. The mantle lithosphere predating metasomatism had the isotopic characteristics of a Depleted Mantle reservoir, possibly formed during Proterozoic depletion events. These DM characteristics of mantle beneath Chenques can be reconciled with the secondary re-crystallised, instead of highly deformed, porphyroclastic texture, shown by xenoliths assuming that the lithosphere underwent in relatively recent times heating-induced re-crystallisation, without addition of exotic components.

The relationships between Sr, Nd isotopes and incompatible trace element concentrations, the relative LILE, HFSE and REE fractionation resulting in high LILE enrichment, Nb and Ti depletion and fractionated REE patterns, all indicate that the metasomatic agent recorded an important signature from the subducted Nazca plate basalts and sediments. The alternative possibility, that metasomatism was operated by alkali basalts similar to that hosting the xenoliths is unsupported by the absence in the basalts of the element fractionations observed in the xenoliths, Also, the specific element anomalies observed in the xenoliths and their equilibrium melts are not likely to have been acquired by reaction between basalts and peridotite, because they are absent in the reactions of basalt veins infiltrating the xenolith.

Since the potential melts in equilibrium with the peridotite clinopyroxenes resemble arc basalts and adakites, we have examined the hypothesis that the Chenques xenoliths represent subarc mantle transported by reversed corner flow 200 km to the East (the distance between arc and Chenques). Since the oldest age of the arc volcanics is Pliocene and Chenques is Quaternary the flow velocity should have been of at least 4 cm $year^{-1}$, which is inconsistent with the lack of deformation textures in the Chenques xenoliths. Therefore, derivation from subarc is unsupported.

The alternative possibility, that the slab signature is a consequence of components released by the slab beneath Chenques (about 200 km deep), is difficult to constrain because of the lack of direct documentation on the mineralogical and chemical transformations along the slab and during percolation in the hidden mantle zone. On the basis of experimental works, we have hypothesised that phengite was the water carrier down to 6 GPa, slab dehydrated, it did not melt before reaching this depth and at 6 GPa phengite breakdown released a high-K, supercritical fluid. Percolations of

these fluids into the hidden mantle induced crystallisation of phlogopite and, at lower pressure, amphibole and during their way up they equilibrated with garnet and clinopyroxene. Comparison of the composition of an estimated slab-derived fluid with that inferred to be the initial metasomatic agent in the xenoliths shows minor differences, consistent with the geochemical variations induced by percolation into the hidden mantle zone. Therefore, in spite of the several poorly constrained assumptions, the hypothesis that the slab signature derives from fluids released under Chenques is our preferred one.

Similarity of the Chenques isotope characteristics with other xenolith occurrences in Northern Patagonia suggest that the recorded geochemical and isotope imprint likely derive from the Nazca plate components. The contrasted compositions with xenoliths from the southern localities situated above the subducted Antarctic plate, although at present poorly documented, suggest that both plates do not have identical isotope composition.

The slab window occurring South of Chenques does not seem to have had any effect on the Chenques mantle composition.

Acknowledgements

J-.L. Bodinier is thanked for having kindly provided the Plate Model software. We are grateful to S.M. Kay for her thorough revision of an earlier version of the manuscript and for having also polished the language. This research was financially supported by the MURST (PRIN funds).

Appendix A. Supplementary materials

Supplementary data associated with this article can be found, in the online version, at doi:10.1016/j.lithos.2007.05.012.

References

Barbieri, M.A., Rivalenti, G., Cingolani, C., Mazzucchelli, M., Zanetti, A., 1997. Geochemical and isotope variability of the northern and southern Patagonia lithospheric mantle. I South Amer. Symposium on Isotope Geology. Extended abstract vol. , pp. 41–43.

Barbieri, M.A., Rivalenti, G., Cingolani, C., Vannucci, R., Kempton, P.D., 1999. Geochemical and isotopic constraints on the composition of the mantle lithosphere in Patagonia (Argentina, Chile). II South Amer. Symposium on Isotope Geology. Extended abstract vol., pp. 163–166.

Bedini, R.M., Bodinier, J.-L., Dautria, Jm.M., Morten, L., 1997. Evolution of LILE-enriched small melt fractions in the lithospheric mantle: a case study from the East African Rift. Earth Planet. Sci. Lett. 153, 67–83.

Bjerg, E.A., Ntaflos, T., Kurat, G., Dobosi, G., Labudia, C.H., 2005. The upper mantle beneath Patagonia, Argentina, documented by xenoliths from alkali basalts. J. South Am. Earth Sci. 18, 125–145.

Brenan, J.M., Neroda, E., Lunstrom, C.C., Shaw, H.F., Ryerson, F.J., Phinney, D.L., 1998a. Behaviour of boron, beryllium, and lithium during melting and crystallization: constraints from mineral-melt partitioning experiments. Geochim. Cosmochim. Acta 62, 2129–2141.

Brenan, J.M., Ryerson, F.J., Shaw, H.F., 1998b. The role of aqueous fluids in the slab-to-mantle tranfer of boron, beryllium, and lithium during subduction: experiments and models. Geochim. Cosmochim. Acta 62, 3337–3347.

Brey, G.P., Köhler, T., 1990. Geothermobarometry in four-phase lherzolites. II. New thermobarometers, and pratical assesment of existing thermobarometers. J. Petrol. 31, 1353–1378.

Cahill, T., Isaks, B.L., 1992. Seismicity and shape of the subducted Nazca plate. J. Geophys. Res. 97, 17503–17529.

Cande, S.C., Leslie, R.B., 1986. Late Cenozoic tectonics of the southern Chile Trench. J. Geophys. Res. 91, 495–520.

Churikova, T., Dorendord, F., Wörner, G., 2001. Sources and fluids in the mantle wedge below Kamchatka, evidence from across-arc geochemical variation. J. Petrol. 42, 1567–1593.

D'Orazio, M., Innocenti, F., Manetti, P., Tamponi, M., Tonarini, S., Gonzàles-Ferran, O., Lahsen, A., Omarini, R., 2003. The quaternary calc-alkaline volcanism of the Patagonian Andes close to the Chile triple junction: geochemistry and petrogenesis of volcanic rocks from the Cay and Maca volcanoes (~45°S, Chile). J. South Am. Earth Sci. 16, 219–242.

Davies, J.H., Stevenson, D.J., 1992. Physical model of source region of subduction zone volcanics. J. Geophys. Res. 97, 2037–2070.

Dorendorf, F., Wieckert, U., Wörner, G., 2000. Hydrated sub-arc mantle: a source for the Kluchevskoy volcano, Kamchatka/Russia. Earth Planet. Sci. Lett. 175, 69–86.

Forneris, J.F., Holloway, J.R., 2003. Phase equilibria in subducting basaltic crust: implications for H_2O release from the slab. Earth Planet. Sci. Lett. 214, 187–201.

Franz, L., Becker, K.-P., Ktamer, W., Herzig, P.M., 2002. Metasomatic mantle xenoliths from the Bismarck Microplate (Papua New Guinea) — thermal evolution, geochemistry and extent of slab-induced metasomatism. J. Petrol. 43, 315–343.

Gorring, M.L., Kay, S.M., 2000. Carbonatite metasomatized peridotite xenoliths from southern Patagonia: implications for lithospheric processes and Neogene plateau magmatism. Contrib. Mineral. Petrol. 140, 55–72.

Gorring, M.L., Kay, S.M., 2001. Mantle processes and sources of Neogene slab window magmas from Southern Patagonia, Argentina. J. Petrol. 42, 1067–1094.

Gorring, M.L., Kay, S.M., Zitler, P.K., Ramos, V.A., Rubiolo, D., Fernandez, M.I., Panza, J.L., 1997. Neogene Patagonian plateau lavas: continental magmas associated with ridge collision at the Chile Triple Junction. Tectonics 16, 1–17.

Green, T.H., Adam, J., 2003. Experimentally-determined trace element characteristics of aqueous fluid from partially dehydrated mafic oceanic crust at 3.0 GPa, 650–770 °C. Eur. J. Mineral. 15, 815–830.

Green, T.H., Blundy, J.D., Adam, J., Yaxley, G.M., 2000. SIMS determination of trace element partition coefficients between garnet, clinopyroxene and hydrous basaltic liquids at 2–7.5 GPa and 1080–1200 °C. Lithos 53, 165–187.

Grégoire, M., McInnes, B.I.A., O'Reilly, S.Y., 2001. Hydrous metasomatism of oceanic sub-arc mantle, Lihir, Papua new Guinea. Part 2: trace element characteristics of slab-derived fluids. Lithos 59, 91–108.

Gutscher, M.-A., 2002. Andean subduction styles and their effect on thermal structure and intraplate coupling. J. South Am. Earth Sci. 15, 3–10.

Hauri, E.H., Wagner, T.P., Grove, T.L., 1994. Experimental and natural partitioning of Th, U, Pb and other trace elements between garnet, clinopyroxene and basaltic melts. Chem. Geol. 117, 149–166.

Hauri, E.H., Gaetano, G.A., Green, T.H., 2006. Partitioning of water during melting of the Earth's upper mantle at H_2O-undersatured conditions. Earth Planet. Sci. Lett. 248, 715–734.

Hermann, J., Green, D.H., 2001. Experimental constraints on high pressure melting in subducted crust. Earth Planet. Sci. Lett. 188, 149–168.

Hickey, R.L., Frey, F.A., Gerlach, D.C., López-Escobar, L., 1986. Multiple sources for basaltic arc rocks from the southern volcanic zone of the Andes (34°–41°S): trace element and isotopic evidence for contributions from subducted oceanic crust, mantle, and continental crust. J. Geophys. Res. 91, 5963–5983.

Hirschmann, M.M., Stolper, E.M., 1996. A possible role for garnet pyroxenite in the origin of the "garnet signature" in MORB. Contrib. Mineral. Petrol. 124, 185–208.

Hofmann, A.W., 1988. Chemical differentiation of the Earth: the relationship between mantle, continental crust, and oceanic crust. Earth Planet. Sci. Lett. 90, 297–314.

Ionov, D.A., Hofmann, A.W., 1995. Nb–Ta–rich mantle amphiboles and micas: implications for subduction-related metasomatic trace element fractionation. Earth Planet. Sci. Lett. 131, 341–356.

Ionov, D.A., Bodinier, J.L., Mukasa, S.B., Zanetti, A., 2002. Mechanisms and sources of mantle metasomatism: major and trace element compositions of peridotite xenoliths from Spitsbergen in the context of numerical modelling. J. Petrol. 43, 1–41.

Kay, S.M., 2002. Magmatic sources, Tectonic setting and causes of tertiary to recent Patagonian plateau magmatism (36°S to 52°S latidude). Actas del XV Congreso Geologico Argentino, El Calafate. Tomo, vol. III, pp. 95–100.

Kay, S.M., Ardolino, A.A., Franchi, M., Ramos, V.A., 1993a. El origen de la meseta de Sumun Cura: distribucion de sus rocas volcanicas maficas. XII Congreso Geologico Argentino y II Congreso de hydrocarburos. Actas I° (IV), pp. 236–248.

Kay, S.M., Ramos, V.A., Marquez, M., 1993b. Evidence in Cerro Pampa volcanic rocks for slab-melting prior to ridge-trench collision in Southern South America. J. Geol. 101, 703–714.

Kay, S.M., Ardolino, A.A., Gorring, M.L., Ramos, V.A., 2007. The Sumuncura large igneous province in Patagonia: interaction of the transient mantle thermal anomaly with a subducting slab. J. Petrology 48, 43–77.

Kelemen, P.B., 1995. Genesis of high Mg# andesites and the continental crust. Contrib. Mineral. Petrol. 120, 1–19.

Kempton, P.D., Hawkesworth, C.J., Lopez-Escobar, L., Pearson, D.G., Ware, A.J., 1999. Spinel±garnet lherzolite xenoliths from Pali Aike: Part 2. In: Gurney, J.J., Gurney, J.L., Pascoe, M.D., Richardson, S.H. (Eds.), Trace element and isotopic evidence bearing on the evolution of lithospheric mantle beneath southern Patagonia. The J.B. Dawson Volume. Proc. International Kimberlite Conference 7, vol. 1, pp. 415–428.

Kepezhiskas, P., Defant, Drummond, M.S., 1996. Progressive enrichment of island arc mantle by melt-peridotite interaction inferred from Kamchatcka xenoliths. Geochim. Cosmochim. Acta 60, 1217–1229.

Kessel, R., Schmidt, M.W., Ulmer, P., Pettke, T., 2005. Trace element signature of subduction zone fluids, melts and supercritical liquids at 120–180 km depth. Nature 437, 724–727.

Kilian, R., Behrmann, J.H., 2003. Geochemical constraints on the sources of Southern Chile trench sediments and their recycling in arc magmas of the Southern Andes. J. Geol. Soc. (Lond.) 160, 57–70.

Kilian, R., Stern, C.R., 2002. Constraints on the interaction between slab melts and the mantle wedge from adakitic glass in peridote xenoliths. Eur. J. Mineral. 14, 25–36.

Kilian, R., Franzen, C., Koch, M., 1998. The metasomatism of the mantle wedge below the southern Andes: constraints from laser ablation microprobe ICP-MS trace element analysis of clinopyroxenes, orthopyroxenes and fluid inclusions of mantle xenoliths. Terra Nostra 98/5, 81–82.

Kinzler, R.J., 1997. Melting of mantle peridotite at pressure approaching the spinel to garnet transition: Application to mid-ocean ridge basalt petrogenesis. J. Geophys. Res. 102, 853–874.

Klein, E.M., Karsten, J.L., 1995. Ocean-ridge basalts with convergent-margin geochemical affinities from the Chile ridge. Nature 374, 52–57.

LaTourrette, T., Hervig, R.L., Holloway, J.R., 1995. Trace element partitioning between amphibole, phlogopite, and basanite melt. Earth Planet. Sci. Lett. 135, 13–30.

Laurora, A., Mazzucchelli, M., Rivalenti, G., Vannucci, R., Zanetti, A., Barbieri, M.A., Cingolani, C.A., 2001. Metasomatism and melting in carbonated peridotite xenoliths from the mantle wedge: the Gobernador Gregores case (Southern Patagonia). J. Petrol. 42, 69–87.

Niida, K., Green, D.H., 1999. Stability and chemical composition of pargasitic amphibole in MORB pyrolite under upper mantle conditions. Contrib. Mineral. Petrol. 135, 18–40.

Ottolini, L., Le Févre, B., Vannucci, R., 2004. Direct assessment of mantle boron and lithium contents and distribution by SIMS analyses of peridotite minerals. Earth Planet. Sci. Lett. 228, 19–36.

Piccardo, G.B., Zanetti, A., Müntener, O., 2007. Melt/peridotite interaction in the Southern Lanzo peridotite: Field, textural and geochemical evidence. Lithos. 94, 181–209.

Ploszkiewicz, J.V., 1987. Descripcion geologica de la hoja 47 c, Apeleg. Direc. Nac. Miner. Geol., Rep. Argentina, Bol., vol. 204, pp. 1–95.

Poli, S., Schmidt, M.W., 1995. H_2O transport and release in subduction zones: experimental constraints on basaltic and andesitic systems. J. Geophys. Res. 100, 2299–2314.

Prouteau, G., Scaillet, B., Pichavant, M., Mauri, R., 2001. Evidence for mantle metasomatism by hydrous silicic melts derved from subducted oceanic crust. Nature 410, 197–200.

Ramos, V.A., Aleman, A., 2000. Tectonic evolution of the Andes. In: Cordani, U.G., Milani, E.J., Thomas Filho, A., Campos, D.A. (Eds.), Tectonic evolution of South America. International Geological Congress, Rio de Janeiro, pp. 635–685.

Ramos, V.A., Kay, S.M., 1992. Southern Patagonia plateau basalts and deformation: backarc testimony of ridge collisions. Tectonophysics 205, 261–282.

Rivalenti, G., Mazzucchelli, M., Laurora, A., Ciuffi, S.I.A., Zanetti, A., Vannucci, R., Cingolani, C.A., 2004a. The backarc mantle lithosphere in Patagonia, South America. J. South Am. Earth Sci. 17, 121–152.

Rivalenti, G., Zanetti, A., Mazzucchelli, M., Vannucci, R., Cingolani, C.A., 2004b. Equivocal carbonatite markers in the mantle xenoliths of the Patagonia backarc: the Gobernador Gregores case (Santa Cruz Province, Argentina). Contrib. Mineral. Petrol. 147, 647–670.

Rivalenti, G., Zanetti, A., Girardi, V.A.V., Mazzucchelli, M., Tassinari, C.C.G., Bertotto, C.W., 2007. The effect of the Fernando de Noronha plume on the mantle lithosphere in north-eastern Brazil. Lithos. 94, 111–131.

Rosenbaum, J.M., Wilson, M., Downes, H., 1997. Multiple enrichment of the Pannonian-Carpathian mantle: Pb–Sr–Nd isotope and trace element constraints. J. Geophys. Res. 102, 14947–14961.

Salters, V.J.M., Longhi, J.E., Bizimis, M., 2002. Near mantle solidus trace element partitioning at pressures up to 3.4 GPa. G^3. doi:10.1029/2001GC000148.

Scambelluri, M., Müntener, O., Ottolini, L., Pettke, T.T., Vannucci, R., 2004. The fate of B, Cl and Li in the subducted oceanic mantle and in the antigorite breakdown fluids. Earth Planet. Sci. Lett. 222, 217–234.

Schmidt, M.W., Poli, S., 1998. Experimentally based water budgets for dehydrating slabs and consequences for arc magma generation. Earth Planet. Sci. Lett. 163, 361–379.

Schmidt, K.H., Bottazzi, P., Vannucci, R., Mengel, K., 1999. Trace element partitioning between phlogopite, clinopyroxene and leucite lamproite melt. Earth Planet. Sci. Lett. 168, 287–299.

Schmidt, M.W., Vielzeuf, D., Auzanneau, E., 2004. Melting and dissolution of subducting crust at high pressures: the key role of white mica. Earth Planet. Sci. Lett. 228, 65–84.

Seyfried, W.E., Janecky, D.R., Mottl, M.J., 1983. Alteration of the oceanic crust: implications for geochemical cycles of lithium and boron. Geochim. Cosmochim. Acta 48, 557–569.

Shaw, C.S., Heidelbach, F., Dingwell, D.B., 2006. The origin of reaction textures in mantle peridotite xenoliths from Sal Island, Cape Verde: the case for "metasomatism" by host lava. Contrib. Mineral. Petrol. 151, 681–697.

Stalder, R.E., Ulmer, P., Thompson, A.B., Gunter, D., 2001. High pressure fluids in the system $MgO–SiO_2–H_2O$ under upper mantle conditions. Contrib. Mineral. Petrol. 140, 607–618.

Stern, C.R., Kilian, R., 1996. Role of the subducted slab, mantle wedge and continental crust in the generation of adakites from the Andean Austral Volcanic Zone. Contrib. Mineral. Petrol. 123, 263–281.

Stern, C.R., Saul, S., Skewes, M.A., Futa, K., 1989. Garnet peridotite xenoliths from Pali-Aike basalts of southernmost South America. Kimberlites and related rocks. . Geol. Soc. Aust., Spec. Publ., vol. 14. Backwell, Carlton, pp. 735–744.

Stern, C.R., Frey, F.A., Futa, K., Zartman, R.E., Peng, Z., Kyser, T.K., 1990. Trace-element and Sr, Nd, Pb, and O isotopic composition of Pliocene and Quaternary alkali basalts of the Patagonia Plateau lavas of southernmost South America. Contrib. Mineral. Petrol. 104, 294–308.

Stern, C.R., Kilian, R., Olker, B., Hauri, E.H., Kyser, T.K., 1999. Evidence from mantle xenoliths for relatively thin (<100 km) continental lithosphere below the Phanerozoic crust of southernmost South America. Lithos 48, 217–235.

Sturm, M.E., Klein, E.M., Graham, D.W., Karsten, J., 1999. Age constraints on crustal recycling to the mantle beneath the southern Chile Ridge: He–Pb–Sr–Nd isotope systematics. J. Geophys. Res. 105, 5097–5114.

Sudo, A., Tatsumi, Y., 1990. Phlogopite and K-amphibole in the upper mantle: implication for magma genesis in subduction zones. Geophys. Res. Lett. 17, 29–32.

Tiepolo, M., Vannucci, R., Oberti, R., Foley, S., Bottazzi, P., Zanetti, A., 2000a. Nb and Ta incorporation and fractionation in Ti-rich pargasite and kaersutite: crystal–chemical constraints and implications for natural systems. Earth Planet. Sci. Lett. 176, 185–201.

Tiepolo, M., Vannucci, Bottazzi, P., Oberti, R., Zanetti, A., Foley, S., 2000b. Patitioning of rare earth elements, Y, Th, U, and Pb between pargasite, kaersutite, and basanite to trachyte melts: implications for percolated and veined mantle. G^3. 2000GC000064.

Tiepolo, M., Bottazzi, P., Palenzona, M., Vannucci, R., 2003. A laser probe coupled with ICP-double-focusing sector-field mass spectrometer for in situ analysis of geological samples and U–Pb dating of zircon. Can. Mineral. 41, 259–272.

Tiepolo, M., Zanetti, A., Vannucci, R., 2005. Determination of Li, Be and B at trace levels by LA–ICP–MS. Geostand. Geoanal. Res. 29, 211–224.

Trua, T., Serri, G., Birkenmajer, K., Pécskay, Z., 2006. Geochemical and Sr–Nd–Pb isotopic composition of the Mts Pieniny dykes and sills (West Carphathians): evidence for melting in the lithospheric mantle. Lithos 90, 57–75.

van Keken, P.E., 2003. The structure and dynamics of the mantle wedge. Earth Planet. Sci. Lett. 6816, 1–16.

van Westrenen, W., Blundy, J.D., Wood, B.J., 2001. High field strength element/rare earth element fractionation during partial melting in the presence of garnet: implications for identification of mantle heterogeneities. G^3. 2000GC000133.

Vernières, J., Godard, M., Bodinier, J.-L., 1997. A plate model for the simulation of trace element fractionation during partial melting and magma transport in the Earth's upper mantle. J. Geophys. Res. 102, 24771–24784.

Wallace, M.E., Green, D.H., 1991. The effect of bulk rock composition on the stability of amphibole in the upper mantle: implications for solidus positions and mantle metasomatism. Mineral. Petrol. 44, 1–19.

White, W.M., Patchett, J., 1984. Hf–Nd–Sr isotopes and incompatible element abundances in island arcs: implications for magma origins and crust-mantle evolution. Earth Planet. Sci. Lett. 67, 167–185.

Xu, Y.G., Menzies, M.A., Bodinier, J.-L., Bedini, R.M., Vroon, P., Mercier, J.-C.C., 1998. Melt percolation and reaction atop a plume: evidence from the poikiloblastic peridotite xenoliths from Borée (Massif Central, France). Contrib. Mineral. Petrol. 132, 65–84.

Yagodzinski, G.M., Kelemen, P.B., 1998. Slab melting in the Aleutians: implications of an ion probe study of clinopyroxene in primitive adakite and basalt. Earth Planet. Sci. Lett. 158, 53–65.

Yaxley, G.M., Green, D.H., 1998. Reactions between eclogite and peridotite: mantle refertilisation by subduction of oceanic crust. Schweiz. Mineral. Petrogr. Mitt. 78, 243–255.

Zanetti, A., Tiepolo, M., Oberti, R., Vannucci, R., 2004. Trace-element partitioning in olivine modelling of a complete data set from a synthetic hydrous basanite melt. Lithos 75, 39–54.